The Thesis committee for Andrew S. Leung

Certifies that this is the approved version of the following thesis:

Forward Modeling of Internal Kinematic Structures of Disk Galaxies in MaNGA

APPROVED BY

SUPERVISING COMMITTEE:

Karl Gebhardt, Supervisor

Niv Drory, Co-supervisor

Michael Boylan-Kolchin

Steven L. Finkelstein

Forward Modeling of Internal Kinematic Structures of Disk Galaxies in MaNGA

by

Andrew S. Leung

Thesis

Presented to the Faculty of the Graduate School

of the University of Texas at Austin

in Partial Fulfillment

of the Requirements

for the Degree of

Master of Arts

The University of Texas at Austin

December 2018

Forward Modeling of Internal Kinematic Structures of Disk Galaxies in MaNGA

by

Andrew S. Leung, MA

The University of Texas at Austin, 2018

Supervisors: Karl Gebhardt
Niv Drory

SDSS-IV MaNGA is a large IFU survey with a goal of observing $\sim 10^4$ galaxies by the survey's end. MaNGA produces spatially resolved kinematic maps that describe the motions of stars and gas in each galaxy, but these maps include the effects of beam smearing. The primary objective of this project is the development, testing and validation of a code designed to accurately extract intrinsic kinematic models from spectroscopic measurements of disk galaxies observed by the MaNGA survey. The code uses a thin disk model including perturbations around circular orbits up to second order to describe bar, spiral and oval features. In this Thesis, we document our implementation of the algorithm and present a small sample of our results to demonstrate the behavior of our code. The code is available online at `http://github.com/aleung12/manga/` under the MIT License.

Table of Contents

Abstract **iii**

Chapter 1. Introduction **1**
1.1 Scientific Motivation . . . 1
1.2 Methodological Motivation . . . 2
1.2.1 Beam Smearing in Astronomical Observations . . . 2
1.2.2 Forward Modeling as the Logical Approach . . . 3

Chapter 2. Data: SDSS-IV MaNGA Survey **5**
2.1 MaNGA IFU Instrument . . . 5
2.2 MaNGA Data Pipeline . . . 6

Chapter 3. Models and Methodology **7**
3.1 Modeling a Kinematic Observation . . . 7
3.1.1 Axisymmetric Model . . . 7
3.1.2 Modeling Nonaxisymmetry . . . 8
3.1.3 Convolution of Signals . . . 10
3.2 Markov Chain Monte Carlo . . . 11
3.2.1 Metropolis–Hastings Algorithm . . . 12
3.2.2 Dynamic Behavior of an MCMC Simulation . . . 13
3.2.3 Parallel Tempering . . . 14
3.2.4 MCMC Design Choices . . . 15
3.2.4.1 Proposal Distributions . . . 15
3.2.4.2 Number of Markov Chains . . . 16
3.2.4.3 Temperature Ladder Specification . . . 16
3.2.4.4 Parallel Tempering Duration . . . 17
3.2.5 Monitoring Convergence . . . 17
3.2.6 Sampling Posterior Distributions . . . 18
3.3 Selection of Galaxy Sample . . . 21

Chapter 4. Results **23**
4.1 Forward Modeling Results: Select Examples . . . 23
4.1.1 A DIsk with Nearly Entirely Circular Motions . . . 23
4.1.2 A Disk with Distinct Velocity Components . . . 27
4.1.3 A Strong Bar Feature . . . 30
4.1.4 Possible Dynamical Heating in Gas Disk . . . 33
4.1.5 Approaching Thin Disk Model's Limit . . . 36
4.1.6 Common Failure Modes . . . 39
4.1.6.1 Convergence but Unphysical . . . 39
4.1.6.2 Failure to Converge . . . 42
4.2 Asymmetric Drift . . . 44
4.3 Tully–Fisher Relation . . . 45

Chapter 5. Conclusion **48**

References **48**

Chapter 1

Introduction

The first-order science goal that motivates this thesis is the use of kinematic measurements to study the dynamical structure of disk galaxies. In order to study the dynamics of galaxies, we need to accurately extract their internal kinematics from spectroscopic observations.[1] In this work, we endeavor to contribute a solution to this antecedent requirement for dynamical study: the development, testing and validation of a code designed to accurately extract kinematic models from spectroscopic measurements of disk galaxies observed by the MaNGA survey.[2].

1.1 Scientific Motivation

Mass-to-light ratio is a fundamental quantity used to describe galaxies, but accurate measurement of the quantity is difficult for a variety of reasons. These include the dependence of mass-to-light (Υ) on galaxies' stellar populations and unique evolution histories, which are poorly understood in general, as well as our understanding of the contribution to the mass content of stellar disks by dark matter halos, which is still not fully developed (Dalcanton & Stilp 2010; Courteau et al. 2014; D'Onghia 2015).

Any dynamical modeling addressing mass-to-light or any other intrinsic property of galaxies requires accurate measurements of the first two kinematic moments, that is, velocity and dispersion fields. Analyses of rotation curves provide strong constraints on the mass distribution of galaxies, while models of velocity dispersion aid the understanding of disk stability and give insight into the mechanics of differentially rotating disks (Bottema 1993). Further, intrinsic kinematic models of stellar and gas components of galaxies provide a means to assess the validity of the asymmetric drift

[1] The ***kinematics*** of a system refer to the observational description of the positions and motions of its constituents, distinct from the system's ***dynamics***, an interpretation of the former in terms of physical laws.

[2] See Chapter 2 for a description of the MaNGA survey (`http://www.sdss.org/surveys/manga/`).

equation, which describes a phenomenon first observed in the solar neighborhood, wherein stars are more likely to lag the local standard of rest than to lead it (Binney & Tremaine 2008; Golubov et al. 2013).

Prior to the advent of integral-field spectroscopy, detailed kinematic studies were restricted to a relatively small sample of the nearest, most-observed galaxies. Kinematic measurements of galaxies were limited by the incompleteness of dimensional coverage. Measurements obtained by long-slit spectroscopy, for example, capture only one spatial dimension (along the slit) and the line-of-sight velocity, from the intrinsically six-dimensional phase space of a galaxy. Some studies have mitigated this problem by taking measurements with the slit oriented in multiple position angles (e.g., Gerssen et al. 1997), but this remedy only comes at the cost of increased requirements for observing time.

Spectrographs with integral-field units (IFU) obtains spectra in two-dimensional fields. As a result of this improvement in dimensional coverage, 2D fields of velocity and velocity dispersion derived from IFU observations contain much more information than long-slit data. 2D data enable us to use higher order models than just circular velocity to describe the velocity field—for example, a thin disk model including perturbations around circular orbits up to second order to describe bar, spiral and oval features. While this increase in dimensional resolution provided by IFU observations enables kinematic study in unprecedented detail, careful handling of observational effects must be undertaken to ensure the correct interpretation of results generated from the data.

1.2 Methodological Motivation

1.2.1 Beam Smearing in Astronomical Observations

Beam smearing is the convolution of a signal by the point spread function (PSF) of the whole system, where the PSF is the output of the system to a delta-function input. Not only is beam smearing a problem that pervades observational astronomy, it is in fact a general problem that is inherent to the measurement and processing of any signal. Just about everything that lies between the emission of a signal and its analysis by an observer has an effect on the quality and accuracy of observed data. These include the medium that the signal passes through and the instrument that

captures of the signal.

Beam smearing due to nonuniform variations in the Earth's atmosphere is most strongly associated with the PSF of an astronomical observation. But natural seeing is just one factor among a host of contributors that affects the response profile of any detector. The dithering pattern of a telescope contributes to beam smearing because it introduces a spatial variation within an observation. In the context of IFU observations, the geometry of IFU fiber aperture and configuration of fibers on the unit are also significant contributors. The intrinsic velocity gradient over the spatial extent of an IFU fiber is observed as a dispersion, which reduces the velocity gradient that is measured and increases the apparent dispersion in the data as a result (Noordermeer et al. 2008; Davies et al. 2011; Varidel et al. 2016). An accurate accounting of all contributions to the total beam of each observation requires detailed modeling. Law et al. (2016) describes the reconstruction of PSF for each MaNGA observation in an overall documentation of the survey's data reduction pipeline.

1.2.2 Forward Modeling as the Logical Approach

To obtain accurate kinematic models free of the effect of beam smearing, we need to remove the observational and instrumental effects captured by PSF reconstruction. Although the literal implementation of the "removal" of these effects points towards the deconvolution of the measurement from the reconstructed PSF, deconvolution is mathematically ill-defined because a unique solution is not guaranteed. If instead we take a forward modeling approach, starting with a kinematic model in intrinsic space and following the signal in the "natural" direction of causality, the model we compare to the observation is a convolution of the intrinsic kinematic signal and the PSF associated with the observation. By taking this forward approach, we simulate the observation by modeling both the intrinsic signal and the cumulative effects of the atmosphere and the detector. This detailed modeling results in a superior representation of the observed data.

For this thesis, we developed a forward modeling code that uses a Markov chain Monte Carlo (MCMC) method to determine the most probable intrinsic models of the first two kinematic moments that best fit the data when the intrinsic signal is convolved with the reconstructed PSF

associated with the observation. To our knowledge, this is the first large-scale study to take a forward modeling approach to remove observational effects in order to recover intrinsic kinematic information from IFU data subject to the effect of beam smearing. The primary goal of the project is to produce accurate intrinsic kinematic models for disk galaxies in MaNGA.

Chapter 2

Data: SDSS-IV MaNGA Survey

Since the SDSS-IV program began in 2014, the **Ma**pping **N**earby **G**alaxies at the **A**pache Point Observatory (MaNGA) survey has utilized modified BOSS spectrographs to produce resolved two-dimensional maps of stellar and gas composition and kinematic structure of galaxies out to 1.5 to 2.5 effective radii (R_e). Two-thirds of MaNGA galaxies are in the 1.5 R_e sample, with the remaining one-third observed by MaNGA out to 2.5 R_e (Wake et al. 2017). The MaNGA sample spans a redshift range $0.02 \lesssim z \lesssim 0.1$, with median redshift $z \sim 0.03$ (Blanton et al. 2017). This unprecedented sample of $\sim 10^4$ galaxies with 2D kinematic data targeted by the end of the survey (Bundy et al. 2015) will provide statistical power unmatched by other existing datasets. The MaNGA dataset is flux-limited sample, with no other selection applied (i.e., no selection by inclination or size). From this sample, targets are chosen such that the survey samples an approximately flat distribution in stellar mass (Wake et al. 2017).

2.1 MaNGA IFU Instrument

To achieve a sample of 10,000 galaxies by the end of the survey, MaNGA observes galaxies simultaneously using 17 pluggable integral-field units (IFUs) with custom aluminum plug plates pre-drilled for each target field. Plugged into each plate in a hexagonal dense pack arrangement are five 127-fiber IFUs, two 91-fiber IFUs, four 61-fiber IFUs, four 37-fiber IFUs, and two 19-fiber IFUs. This was found to be the optimal distribution of IFU sizes given the apparent size distribution of nearby galaxies (Drory et al. 2015). Measurements obtained by the MaNGA IFU instrument generate spectroscopic maps over the wavelength range of 3600–10000 Å with spectral resolution $R \sim 2500$ (Drory et al. 2015).

2.2 MaNGA Data Pipeline

The MaNGA Data Reduction Pipeline (DRP; Law et al. 2016) provides reconstructed PSFs for each observation. The MaNGA Data Analysis Pipeline (DAP; Westfall et al., in preparation) produces 2D velocity and dispersion maps, among other science data products, based on spatially resolved spectroscopic measurement ("data cube") of each galaxy. Gas kinematics correspond to observations in the 22 emission line channels of MaNGA, with motions of gas encoded in the profiles of the emission lines. Stellar kinematics are measured by the penalized pixel-fitting code[1] pPXF (Cappellari & Emsellem 2004) with stellar templates from the MILES library (Sánchez-Blázquez et al. 2006). Results reported in Section 4 are based on data from the sixth MaNGA Product Launch (MPL-6).

[1]The MaNGA Data Analysis Pipeline (DAP) has many proprietary changes to the public version of pPXF.

Chapter 3

Models and Methodology

In order to study the dynamics of galaxies, we need to accurately extract their internal kinematics from spectroscopic observations. The accuracy of any modeled kinematic results is inextricably linked to careful accounting of contributions to beam smearing and the removal of their cumulative effect, which we achieve by taking a forward modeling approach. In this chapter, we discuss our choice of kinematic models, the forward modeling framework in detail, and, in general terms, the observed attributes of galaxies for which our method is appropriate.

In Section 3.1, we examine rotational motion in disk galaxies and descriptions of this motion by kinematic models with different assumptions and complexities, and the relationship between the intrinsic signal and the measured data. In Section 3.2, we construct a Markov chain Monte Carlo (MCMC) algorithm designed to recover intrinsic models of the first two kinematic moments from IFU data. We also document some design choices as well as the considerations that drove them. In Section 3.3, we discuss assumptions and the limitations of this forward modeling method taken as a whole and provide a general description of the initial sample of MaNGA galaxies selected to test and validate the code.

3.1 Modeling a Kinematic Observation

3.1.1 Axisymmetric Model

The kinematics of a system refer to the observational description of the positions and motions of its constituents. Our forward modeling approach require some description of the kinematic moments of interest. A basic axisymmetric rotational model for the first kinematic moment (velocity) is given by

$$V_{\rm model}(R,\theta) = V_{\rm sys} + V_\theta(R)\,\sin i\,\cos\theta\,, \tag{3.1}$$

where $V_\theta(R)$ is the one-dimensional rotation curve, which describes average bulk tangential motion as a function of distance from the rotational axis; i is inclination, the angle between the plane of the disk and the plane of the sky; θ is azimuthal angle in the galaxy plane. A common parametrization (e.g., Andersen & Bershady 2013) for the intrinsic rotational speed is

$$V_\theta(R) = V_{\rm max}\, \tanh(R/h_{\rm rot})\,. \tag{3.2}$$

As a function of R, the radial coordinate in the plane of the disk galaxy, this model rotation curve takes the form of a sigmoid function, governed by the hyperbolic tangent term, with velocity rising from zero at a galaxy's center to $\pm V_{\rm max}$ for $|R| \gg h_{\rm rot}$. In Equation 3.1, $\sin i$ captures the line-of-sight component of a velocity vector along the projected major axis. $V_\theta(R)\sin i$ is therefore the observed rotational speed. Azimuthal angle θ is measured from the projected major axis (the angular position in the galaxy plane that corresponds to the position angle of the major axis we measure in the sky), so $\cos\theta$ maps the 1D model along the major axis to different spatial locations in the disk. $V_{\rm sys}$ is the systemic velocity of the galaxy, the rate at which the entire disk is moving along the line-of-sight direction; mathematically, $V_{\rm sys}$ represents a scalar offset for the entire 2D velocity map.

3.1.2 Modeling Nonaxisymmetry

The assumption of axisymmetry can be violated in galaxy disks by bar, oval or spiral structures. Any such noncircular motions in the disk requires a kinematic model that take into account non-axisymmetric flows caused by bar-like or oval distortions to the potential. Taking a Fourier series expansion around a circular orbit with radius R and truncating after the $m = 2$ terms[1] , we obtain

$$V_{\rm model}(R,\theta) = V_{\rm sys} + \sin i\left[\bar{V}_t\cos\theta - V_{2,t}\cos(2\theta_b)\cos\theta - V_{2,r}\sin(2\theta_b)\sin\theta\right]\,, \tag{3.3}$$

where

$$\theta_b \equiv \theta - \phi_b \tag{3.4}$$

[1]By assuming axisymmetry, we are setting the $m = 1$ term to zero.

and ϕ_b is the axis of the $m = 2$ distortion ("bar axis") in the galaxy plane, measured from the projected major axis (the angular position in the galaxy plane that corresponds to the ϕ_0 we measure in the sky). Therefore, θ_b is an azimuthal angle in the galaxy plane relative to the bar axis.

As with any Fourier series expansion, we can model as many terms in the infinite series as is appropriate for the application of interest (Krajnović et al. 2006; Spekkens & Sellwood 2007). In this Fourier interpretation, m describes the periodicity of a particular term. The axisymmetric model in Equation 3.1 is exactly the Fourier series in which all terms higher than $m = 0$ are zero; in other words, a model with no departure from pure circular motion. The model described by Equation 3.3 retains the $m = 2$ terms from the Fourier series in addition to the $m = 0$ circular term. Therefore, this model allows for motions that depart from circular motion with $m = 2$ periodicity over the course of an orbit; Spekkens & Sellwood (2007) refers to Equation 3.3 as a bisymmetric model. These departures from circular motion result from $m = 2$ distortions to the potential, which may result in bars, grand design spirals (two arms) and ovals. The magnitude of the coefficients associated with these terms describe the strength of these perturbations to the mean tangential speed $\bar{V}_t$.

This bisymmetric velocity model has four parameters that describe the orientation and systemic motion of the disk and three parameters that give the magnitude of the velocity terms.

Global parameters. $V_{\rm sys}$ is systemic velocity; in the present application, this is relative to the output of the MaNGA Data Reduction Pipeline (DRP; Law et al. 2016). i is inclination angle of the disk; $i = 0$ and $i = \pi/2$ correspond to face-on and edge-on orientations, respectively. ϕ_0 is position angle of the projected major axis in the plane of the sky. ϕ_b is position angle of the bisymmetric distortion from the deprojected major axis in the plane of the disk.

Radial dependence. $\bar{V}_t$ is the mean tangential velocity, the coefficient on the zeroth-order term in the Fourier series expansion. $V_{2,t}$ and $V_{2,r}$ are the coefficients on the tangential and radial components of $m = 2$ terms and describe nonaxisymmetric motions. For the second kinematic moment (velocity dispersion), we assume isotropy and only model the line-of-sight component of

dispersion as a function of distance from the rotational axis:

$$\sigma_{\rm model}(R, \theta) = \sigma_{_V}(R)\,. \tag{3.5}$$

Radius and azimuthal angle in plane of the galaxy disk (R, θ) are related to their corresponding quantities on the plane of the sky (r, ϕ) by the geometry of projection (inclined view of a circular disk):

$$\tan\theta = \tan(\phi - \phi_0)\cos i \tag{3.6}$$

and

$$R = r\cos(\phi - \phi_0)\cos\theta\,, \tag{3.7}$$

where ϕ_0 is the position angle of the projected major axis in the sky and i is the disk inclination, as before. Projections between 1D radial profiles and 2D maps follow Equation 3.1. We interpolate linearly between bin centers so that every pixel has a corresponding model value.

For dispersion data, MaNGA MPL-6 provides instrumental corrections ($\sigma_{\rm inst}$). The measured dispersion (reported by MaNGA DRP) is the quadrature sum of the observed dispersion and the instrumental correction. Put differently, the dispersion we wish to model is given by

$$\sigma_{\rm obs} = \sqrt{\sigma^2_{\rm meas} - \sigma^2_{\rm inst}}\,. \tag{3.8}$$

If $\sigma_{\rm meas} < \sigma_{\rm inst}$, we mask the pixel. Before fitting, we additionally mask any pixel where the reported inverse variance IVAR $< 10^{-4}$ (km s^{-1})$^{-2}$, corresponding to measurement uncertainty > 100 km s^{-1}.

3.1.3 Convolution of Signals

These intrinsic kinematic models projected to the plane of the sky, described above in Section 3.1, must undergo a most crucial step before they can be directly compared to the observed data, which are degraded by beam smearing.

The MaNGA Data Reduction Pipeline (DRP) reconstructs the PSF corresponding to each observation. Each reconstructed PSF captures the natural seeing beam smearing, fiber geometry, dithering pattern, and the algorithm involved in reconstructing the data cube (Law et al. 2016).

The profile of the reconstructed PSF varies among observations; in general, the FWHM is $\sim 2.5''$. To obtain observed kinematic models, we convolve the intrinsic models with the PSF as follows:

$$V_{\rm obs}(\vec{x}) = \frac{\int V_{\rm intr}(\vec{x}-\vec{x}')\, F(\vec{x}-\vec{x}')\, {\rm PSF}(\vec{x}')\, d\vec{x}'}{\int F(\vec{x}-\vec{x}')\, {\rm PSF}(\vec{x}')\, d\vec{x}'}\,, \tag{3.9}$$

$$\sigma^2_{\rm obs}(\vec{x}) = \frac{\int \left(\sigma^2_{\rm intr}(\vec{x}-\vec{x}') + (V_{\rm intr}(\vec{x}-\vec{x}') - \bar{V}(\vec{x}))^2\right)\, F(\vec{x}-\vec{x}')\, {\rm PSF}(\vec{x}')\, d\vec{x}'}{\int F(\vec{x}-\vec{x}')\, {\rm PSF}(\vec{x}')\, d\vec{x}'}\,. \tag{3.10}$$

In each case, the kinematics are weighted by the flux associated with the measurement prior to convolution, reflecting the nature of signal carried by photons, and finally normalized. For dispersion, the quantity convolved with the PSF is the quadrature sum of the intrinsic velocity dispersion and the intrinsic velocity gradient. Equation 3.10 captures the way in which the intrinsic velocity model affects the observed velocity dispersion; this is the beam smearing effect that we wish to remove from the observed data by forward modeling in order to obtain intrinsic kinematic quantities.

Using the $\otimes$ symbol to denote convolution and normalization, Equations 3.9 and 3.10 may be written in a more compact form:

$$V_{\rm obs} = (V_{\rm intr} \cdot {\rm flux}) \otimes {\rm PSF}\,, \tag{3.11}$$

$$\sigma^2_{\rm obs} = \left(\left[\sigma^2_{\rm intr} + (V_{\rm intr} - \bar{V})^2\right] \cdot {\rm flux}\right) \otimes {\rm PSF}\,. \tag{3.12}$$

3.2 Markov Chain Monte Carlo

We developed a Markov chain Monte Carlo (MCMC) code specifically designed to fit MaNGA data to our kinematic models, taking into account the reconstructed PSF for each observation. The choice of MCMC for this application was driven by several practical considerations. Primarily, MCMC is a natural implementation of the forward modeling concept, which allows us to proceed without having to attempt deconvolution of the observed data from reconstructed PSFs, a process that is mathematically degenerate. Moreover, MCMC serves our objective to sample the posterior for each parameter in our models, as opposed to merely identifying a single set of best-fit model parameters.

To avoid overfitting the data, we cannot model individual pixels. In theory, since the signals reported in pixels separated by less than one full-width-at-half-maximum (FWHM) of the PSF are

correlated, the size of a bin in the model must be $\gtrsim \frac{1}{2}\times$ the PSF FWHM. This is a statement of the Nyquist sampling theorem (Press et al. 2007).

For each galaxy in question, we initialize an intrinsic velocity model with axisymmetric rotational speeds (Equation 3.1). We also initialize an intrinsic velocity dispersion model according to Equation 3.5. Next, we project each model onto the sky and convolve these initial models with the reconstructed PSF associated with the observation and compute χ^2 for these initial models by comparing the convolved models to the corresponding kinematic data.

3.2.1 Metropolis–Hastings Algorithm

Markov chain Monte Carlo (MCMC) is class of statistical methods used realize a random sample from a probability distribution with unknown analytical form (often a complicated multidimensional integral). The Metropolis–Hastings algorithm is the most fundamental MCMC method for sampling from a posterior distribution.

In each MCMC iteration, we select a parameter at random and propose a new value, drawing from a symmetric distribution centered at the current parameter value. We generate a new 2D model based on the proposed parameters (only one was updated), convolve with the model with the PSF according to Equations 3.9 and 3.10 and update χ^2.

At any given iteration and for a state $\vec{\theta}_i$ representing the current position of the Markov chain in parameter space, a proposed transition to the next state $\vec{\theta}_{i+1}$ is accepted with probability

$$A_{\vec{\theta}_i \to \vec{\theta}_{i+1}} = \min \left\{ 1, \frac{\pi(\vec{\theta}_{i+1})}{\pi(\vec{\theta}_i)} \frac{q(\vec{\theta}_i|\vec{\theta}_{i+1})}{q(\vec{\theta}_{i+1}|\vec{\theta}_i)} \right\}, \tag{3.13}$$

where π is the posterior distribution and q is the proposal distribution, whose form is arbitrary (Ivezić et al. 2014), but a distribution that is symmetrical about the current value of the parameter is generally the most convenient choice because transition probabilities in the forward and reverse directions are equal.

If the proposed transition in parameter space results in a smaller value of χ^2, the code accepts the proposal and the MCMC walker advances to the new state in parameter space. Otherwise,

the proposed transition is accepted with probability $e^{-(\chi^2_{i+1}-\chi^2_i)}$. This is a Metropolis–Hastings algorithm in which the likelihood function is given by the tail of the χ^2 distribution and the proposal distribution is symmetric. As the MCMC algorithm proceeds, in each iteration it selects a parameter at random and marginalizes over the remaining parameters (which are held fixed in the current iteration); this is known as Gibbs sampling.

The Metropolis–Hastings algorithm performs poorly if the target distribution we wish to sample is multimodal: if an MCMC walker is too likely to accept proposed transitions, the random sample realized by the Markov chain not representative of the target distribution; if it is too unlikely to accept proposed transitions, the rate of sampling is inefficient at best, or, worse, the chain gets stuck in local regions of high posterior probability and fails to explore the entire prior volume, or requires an inordinately large number of iterations to do so.

3.2.2 Dynamic Behavior of an MCMC Simulation

Monte Carlo methods are iterative simulations. When considering models with a large number of parameters, constructing an efficient MCMC algorithm involves some competing considerations.

Starting with a generic model, corresponding to a reasonable location in parameter space, we want to the algorithm to reach the high-probability density region of the joint posterior distribution as quickly as possible. The theoretical optimal acceptance rate for proposed transitions in MCMC simulations is 23.4% under general conditions (Roberts et al. 1997). In practice when working with a large number of model parameters, the acceptance rates associated with individual parameters will vary greatly over the course of a simulations due to the correlation of model parameters describing a physical system. In the case of kinematic signal from a rotating disk galaxy, the orientation of the disk determines the magnitude of the line-of-sight component of velocity. Thus, a proposed transition to update, for instance, the inclination angle must be at least somewhat compatible with the current values of all velocity parameters in order to be accepted. This favors the proposal of small transition steps.

We want the algorithm to explore the entire joint posterior distribution. Once the algorithm

reaches a region of high probability density, we want the mode explored as efficiently as possible. This favors larger transition steps. We also want to ensure that the algorithm is able to escape any local maxima it encounters. This favors even more aggressive transition proposals.

Deploying multiple Markov chains to independently sample the joint posterior distribution is a helpful but incomplete solution. This mitigates the problem stemming from the natural limitation of an individual chain being only able to occupy one model state at a time. Taken as a system, the set of all chains is thus able to move in independent directions and simultaneously explore vastly different regions of the parameter space. However, the problem of getting stuck in local maxima in the joint posterior remains for any individual chain independently exploring parameter space.

3.2.3 Parallel Tempering

A technique known as parallel tempering can reduce long correlation times typical of standard Monte Carlo methods. Swendsen & Wang (1986) are credited with the technique's first application to modeling physical systems.[2] The idea is to use multiple Markov chains to simultaneously sample the target distributions at different "temperatures." Each MCMC walker is assigned a different temperature T, corresponding the likelihood function raised to the $1/T$ power. The posterior distribution "seen" by a *tempered* Markov chain exploring parameter space at temperature T is given by

$$\pi_{_T}(\vec{\theta}) \propto L(\vec{\theta})^{1/T} p(\vec{\theta})\,, \tag{3.14}$$

where $\vec{\theta}$ is the chain's position in parameter space, L is the likelihood function, and p is the prior probability.

In parallel-tempered MCMC, "swaps" between adjacent chains are proposed at predetermined intervals. Proposed swaps are accepted with probability

$$A_{i\leftrightarrow j} = \min\left\{1, \left(\frac{L(\vec{\theta}_i)}{L(\vec{\theta}_j)}\right)^{\frac{1}{T_j}-\frac{1}{T_i}}\right\}, \tag{3.15}$$

where L is the likelihood function at parameter space position $\vec{\theta}$, and $T_i < T_j$.

[2] The technique's originators referred to it as *replica exchange sampling*.

At predetermined intervals (10,000 proposed transitions in each chain), we consider the values of χ^2 corresponding to the location in parameter space inhabited by every pair of chains with adjacent temperatures, starting with the pair with the two highest temperatures. In this manner, the parameter vector corresponding to the smallest value of χ^2 among all the chains is always taken up by the untempered $T = 1$ walker at the beginning of the next iteration. The cold chains thereby gain access to the entire prior volume, with the $T = 1$ chain sampling the actual target distribution. The posterior distribution π is smoothed out for increasing values of T, since the likelihood raised to a power of inverse temperature ($0 < 1/T < 1$) renders individual peaks in L are flatter and broader.

The untempered cold chain ($T = 1$) gains access to all modes of the posterior π via swaps, which are proposed at predetermined intervals, provided that the temperature ladder specification and the choice of $T_{\max}$ are appropriate. The spacing between adjacent temperatures must be sufficiently small so that, in the case of two adjacent chains where the cold chain is in a better position (smaller value of χ^2) than the hot chain, a proposed swap is not rejected 100% of the time (see Equation 3.15). Furthermore, the chosen $T_{\max}$ must be appropriately large such that the hottest chain can access all modes of π (Vousden et al. 2016).

3.2.4 MCMC Design Choices

3.2.4.1 Proposal Distributions

Adopting a uniform distribution for the proposal distributions is assumption-free. Given a current value for a model parameter and a uniform proposal distribution, a proposed transition to all values falling within a finite distance[3] from the current parameter value are equally likely. Though of course the probability that such proposals will be accepted are not equal, which means the choice of uniform proposal distributions is inherently inefficient because such proposed transitions are not more likely to keep the chain close to its current position when it is already in a good state.

We opted for Gaussian (normal) distributions as the more natural choice for proposals due to its

[3]The abrupt endpoints of the uniform distribution are another source of problems when used as proposal distributions.

concentration of probability density around the current value of the parameter under consideration, which serves as the mean of the Gaussian. In addition, Gaussian proposals retain the convenient property of symmetry about the current parameter value.

Table 3.1 – Values of (Gaussian) σ characterizing the width of proposal distribution for each model parameter

Model parameter	Scope	Proposal σ
$\bar{V}_t$	Radial bin	1 km s^{-1}
σ_V	Radial bin	1 km s^{-1}
$V_{2,t}$	Radial bin	1 km s^{-1}
$V_{2,r}$	Radial bin	1 km s^{-1}
$V_{\rm sys}$	Global	0.5 km s^{-1}
i	Global	0.5°
ϕ_0	Global	0.5°
ϕ_b	Global	0.5°

The acceptance rate of proposed transitions is governed by the width or spread of the proposal distributions. Table 3.1 summarizes the empirical choices for the values of standard deviation σ of the Gaussian distributions from which we realize transition proposals for each model parameter.

3.2.4.2 Number of Markov Chains

Taking into account the interplay between the particulars of the data and several practical considerations involving computational constraints—and much experimentation and testing—we chose to allocate 20 cores to forward model the kinematics of each MaNGA galaxy. This involves devoting 10 chains to model the kinematics of stars and 10 chains to model gas kinematics.

3.2.4.3 Temperature Ladder Specification

We adopt a geometrically-spaced temperature ladder for the parallel-tempering phase of our MCMC code, with temperatures for the 10 chains given by

$$T \in \{10^0, 10^{0.1}, 10^{0.2}, ..., 10^{0.8}, 10^{0.9}\} = \{1.0, 1.259, 1.585, ..., 6.310, 7.943\}\,.$$

3.2.4.4 Parallel Tempering Duration

Finally, we must choose how to allocate computing time between the parallel tempering phase and the sampling phase of our MCMC method. In our application, the goal of parallel-tempered MCMC is to optimize the search for a good location in parameter space from which to begin sampling the true posterior in order to maximize the eventual MCMC sample.

In effect, the parallel tempering phase of our MCMC code serves to establish a new, better-than-generic initial model using only 20 swap iterations (or 200,000 proposed transitions in total, for each chain). Thereafter, all chains sample the untempered ($T = 1$) posterior distribution using the position of the $T = 1$ chain after the 20 swap proposals as the initial model. Switching off parallel tempering at this point in the method in favor of devoting more computing resource to sampling the posterior reflects the severely diminished returns of the hot chains after 20 swap opportunities. A chain with smaller χ^2 always moves down the temperature ladder, with the best (smallest) χ^2 always moves to the coldest ($T = 1$) chain. Once the $T = 1$ chain has reached a set of parameter values that is located in the vicinity of the global maximum of the joint posterior distribution and is looking for improvement from there, it becomes increasing unlikely that chains sampling tempered distributions will be able to find a set of parameters that results in successful swaps all the way down to $T = 1$.

Given the set of parameter values that characterize the proposal distributions (their widths, given by σ of the Gaussian proposal distribution; see Table 3.1) for each parameter in the kinematic model, optimized so that the overall acceptance rate for proposed transitions is $\sim 23\%$ at $T = 1$, we identified 20 swap iterations to be a conservative configuration that enables the vast majority of MaNGA disk galaxies with good signal-to-noise to proceed to the sampling phase in good position to efficiently sample the posterior at $T = 1$.

3.2.5 Monitoring Convergence

The MCMC sample is obtained from the final portions of chains sampling at $T = 1$ that have long since converged to the true posterior in most cases. To verify this convergence, we define a

quantity $\hat{r}$ ("potential scale reduction factor"), following Gelman & Shirley (2011), as the square root of the ratio of the variance of the posterior distribution for a parameter sampled by all chains ("mixture variance") to the average variance of the posterior distribution for the parameter sampled by each chain ("average within-chain variance"):

$$\hat{r} \equiv \sqrt{\frac{\mathrm{var}(\{p_1, p_2, ..., p_n\})}{\frac{1}{n}\sum_{i=1}^{n} \mathrm{var}(p_i)}}\,, \tag{3.16}$$

where p represents sampled values of the parameter in question and n is the number of Markov chains. We require $\hat{r} < 2$ for all fitted parameters in order for a galaxy's results to be included in the samples for the analyses to be presented in Sections 4.2 and 4.3. Proceeding with utmost caution, we exclude the results for a galaxy due to mere possibility of poor fit if *any* parameter fails to converge.

Figure 3.1 shows the progression of $\hat{r}$ associated with each fitted model parameter during an MCMC fit for the stellar kinematics of MaNGA galaxy 8249-12704. In this example, all parameters have converged. Convergence is not equivalent to having generated a robust MCMC sample, however, so the algorithm must continue to iterate after the chains are deemed to have converged numerically.

3.2.6 Sampling Posterior Distributions

In order to draw a statistical sample from the MCMC posterior for each fitted parameter, we need to ensure that the parameter space is well-explored at $T = 1$. Parallel tempering optimizes the initial exploration of the parameter space by allocating computing resources to $T > 1$ chains, at the expense of time spent sampling the untempered target distribution. Since the MCMC sample can only derive from $T = 1$ chains, we turn off parallel tempering after it has served its purpose. Conservatively calibrated to perform on disk galaxies in MaNGA, the code switches to sampling at $T = 1$ with all available chains after 200,000 proposed transitions (per chain), corresponding to 20 iterations of swap proposals. To generate an MCMC sample, we sample every third accepted value for each fitted parameter from the last 300,000 proposed MCMC transitions in each chain. All Markov chains have been sampling at $T = 1$ since parallel tempering was turned off, for the last

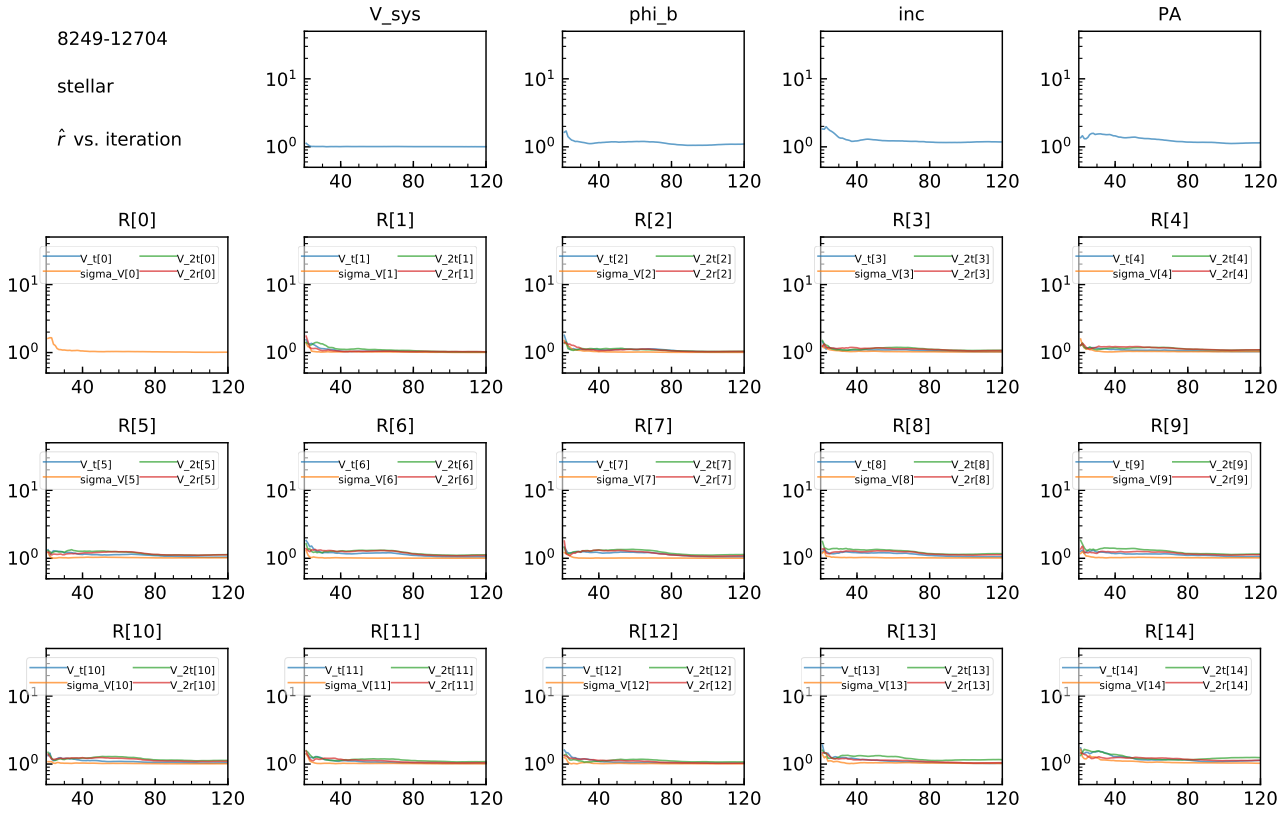

Figure 3.1 – The "potential scale reduction factor," $\hat{r}$, associated with each fitted model parameter for the stellar kinematics of MaNGA galaxy 8249-12704. $\hat{r} \to 1$ indicates the convergence of a model parameter.

1,000,000 proposed transitions.

Figure 3.2 shows the posterior distributions of model parameters for the stellar kinematics of MaNGA galaxy 8249-12704, sampled by each of the 10 MCMC walkers during the course of 1,000,000 proposed transitions following the end of the parallel tempering phase. For the majority of the fitted parameters, the posterior distributions sampled by the 10 chains overlap almost exactly. For those parameters that do not pass this "eye test," Figure 3.1 confirms that they have indeed converged. Convergence requires that all Markov chains sampling the posterior distribution experience the nearly the same variance (see Equation 3.16), and does not require that they result in identical distributions. Indeed, these parameters illustrate the rationale for sampling in parallel using an ensemble of Markov chains. The total sample obtained by the ensemble of MCMC walkers reflects the algorithm's best determination of the true posterior distribution given the observed data. This is in fact the essence of MCMC.

3.3 Selection of Galaxy Sample

The initial sample of MaNGA galaxies, for the purpose of developing and testing our MCMC code, was selected for morphology and inclination angle of the disk. Rotating disks exhibit a characteristic "spider diagram" pattern in 2D maps of line-of-sight velocity. Smoothly varying spider diagrams (as opposed to those that appear "blotchy") are naturally easier to fit to the relatively simple velocity models described in Section 3.1.

Circular motion in the plane of a face-on disk ($i \sim 0°$) does not have a line-of-sight component; velocity measurements of face-on systems are dominated by random motions. As $i \to 0°$, so too does the line-of-sight signal from motions in the plane of the disk, since the signal is proportional to $\sin i$. A disk with edge-on orientation ($i \sim 90°$) does not project into the plane of the sky. As $i \to 90°$, the assumption of an infinitely thin disk model becomes increasingly problematic for two reasons: any line-of-sight traces through a large range of radii in a thick disk (different values of R in cylindrical coordinates), and our models do not currently consider a central bulge.

Therefore, galaxies are selected for strong rotational signature and restricted to intermediate inclinations ($20° \lesssim i \lesssim 70°$) for the purpose of developing and testing the performance of our MCMC code. This selection is not intended to produce a representative sample of nearby galaxies, a requirement that the overall MaNGA sample is designed to achieve (Wake et al. 2017).

We utilized the Marvin webtool developed by Cherinka et al. (2018) to identify galaxies that our code is likely to model successfully by visual inspection of the SDSS optical image and 2D kinematic maps from the MaNGA DAP (Westfall et al., in preparation).

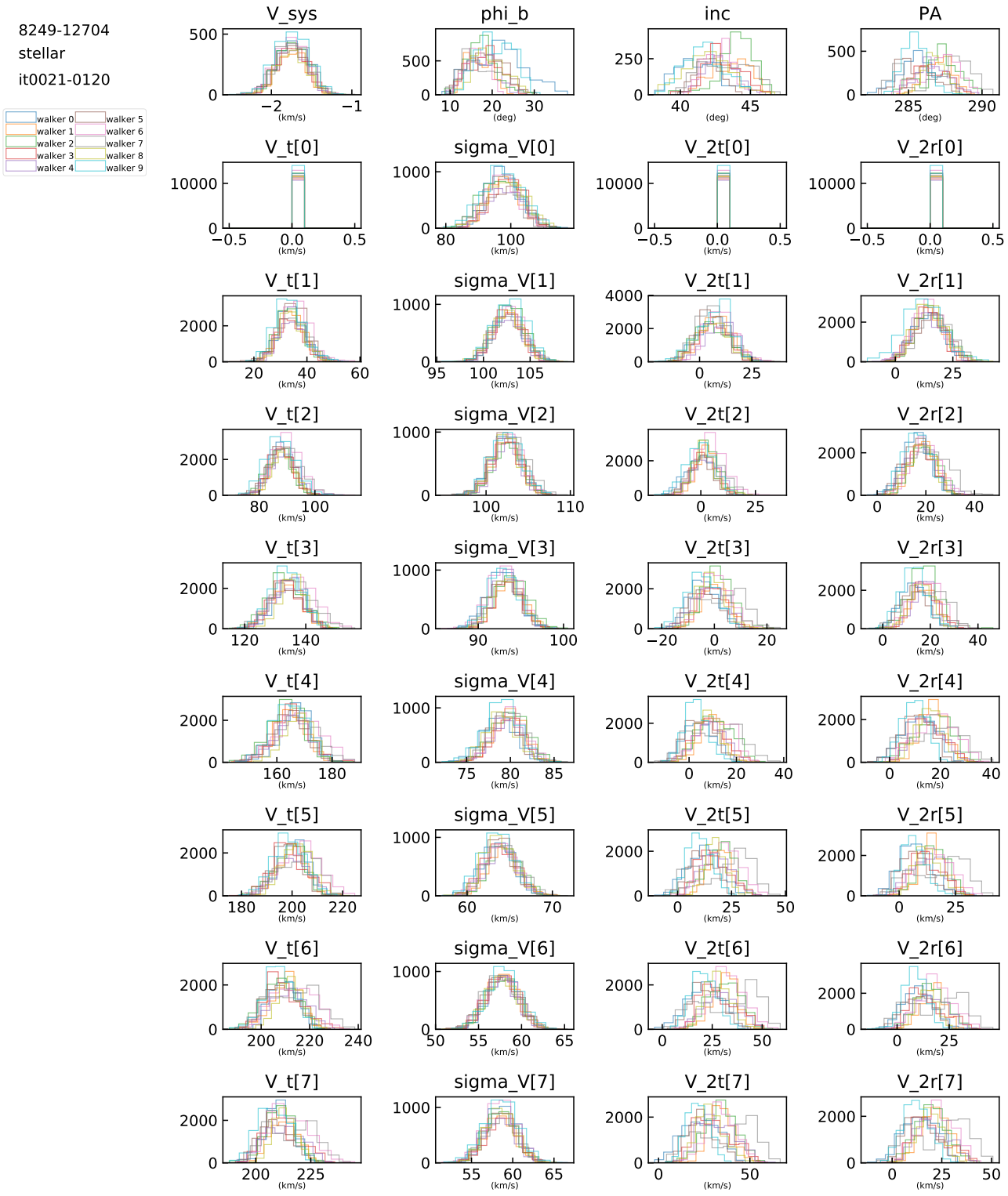

Figure 3.2 – The posterior distributions obtained by 10 MCMC walkers during the course of 1,000,000 proposed transitions following the end of the parallel tempering phase of our MCMC code, for 36 of the fitted parameters in the stellar kinematic model for MaNGA galaxy 8249-12704. Note that $\{\bar{V}_t, V_{2,t}, V_{2,r}\}$ at $R = 0$ are fixed at zero (not fitted). Also note that convergence is not equivalent to a requirement that all walkers discover identical posterior distributions (see Equation 3.16 and discussion in Section 3.2.6). The total sample obtained by the ensemble of MCMC walkers reflects the algorithm's best determination of the true posterior distribution given the observed data.

Chapter 4

Results

4.1 Forward Modeling Results: Select Examples

In this section, we present detailed results of our MCMC fitting on select MaNGA disk galaxies. These results are intended to demonstrate the performance of the code, including its ability to quantify kinematic structures that correspond to observed features readily identifiable in optical imaging. We also include a short discussion on common failure modes that may or may not come as surprises.

4.1.1 A DIsk with Nearly Entirely Circular Motions

Figures 4.1 and 4.2 show the data and fitted kinematic results for MaNGA galaxy 8249-12704. The intrinsic models in the right-most column are convolved with the reconstructed PSF according to Equations 3.9 and 3.10 to produce the observed models shown in the second column. Subtracting the latter from the MaNGA kinematic data, shown in the first column, yields the model residuals shown in the third column. Corresponding 2D maps of χ^2 are shown in the fourth column.

The error bars on binned 1D data (in the indicated top row panels) represent 1-sigma uncertainty on binned measurements, calculated as the quadrature sum of two RMS quantities: a sigma contributed by pixels in the bin and a sigma that captures the variance of data in the bin.

$$\sigma_{\rm bin} = \sqrt{\langle \sigma_m^2 \rangle + \langle \sigma_n^2 \rangle}\,, \tag{4.1}$$

where σ_m denotes the measurement uncertainty associated with a pixel (σ_m^2 is the inverse of the IVAR reported in MPL-6) and σ_n^2 captures the variance in the binned data, computed as the difference to between the data value at a given pixel and the average value of its four adjacent pixels.[1] The error

[1]The errors on fitted inclination and position angles should be propagated through, but these errors are comparatively small and their negligible contributions will not visibly alter the error bars shown in the 1D figures.

bars on binned 1D model quantities represent 1σ (thick) and 2σ (thin) of the posterior distributions sampled by MCMC.

In SDSS optical imaging, this object appears to an S0 or Sa galaxy oriented at a moderate angle of inclination. The 2D MaNGA velocity data for both its stellar and gas components exhibit near-ideal "spider diagram" patterns, indicating nearly unperturbed circular rotation. Our MCMC-fitted kinematic results appear to confirm this. The intrinsic stellar velocity model shows the $m = 2$ terms are very weak or consistent with zero at all modeled radii. In the intrinsic gas velocity model, the $m = 2$ terms depart more significantly from zero in the central $5''$, though still quite weak compared to the mean rotation speed. This feature likely corresponds to a weak bulge near the center of the galaxy.

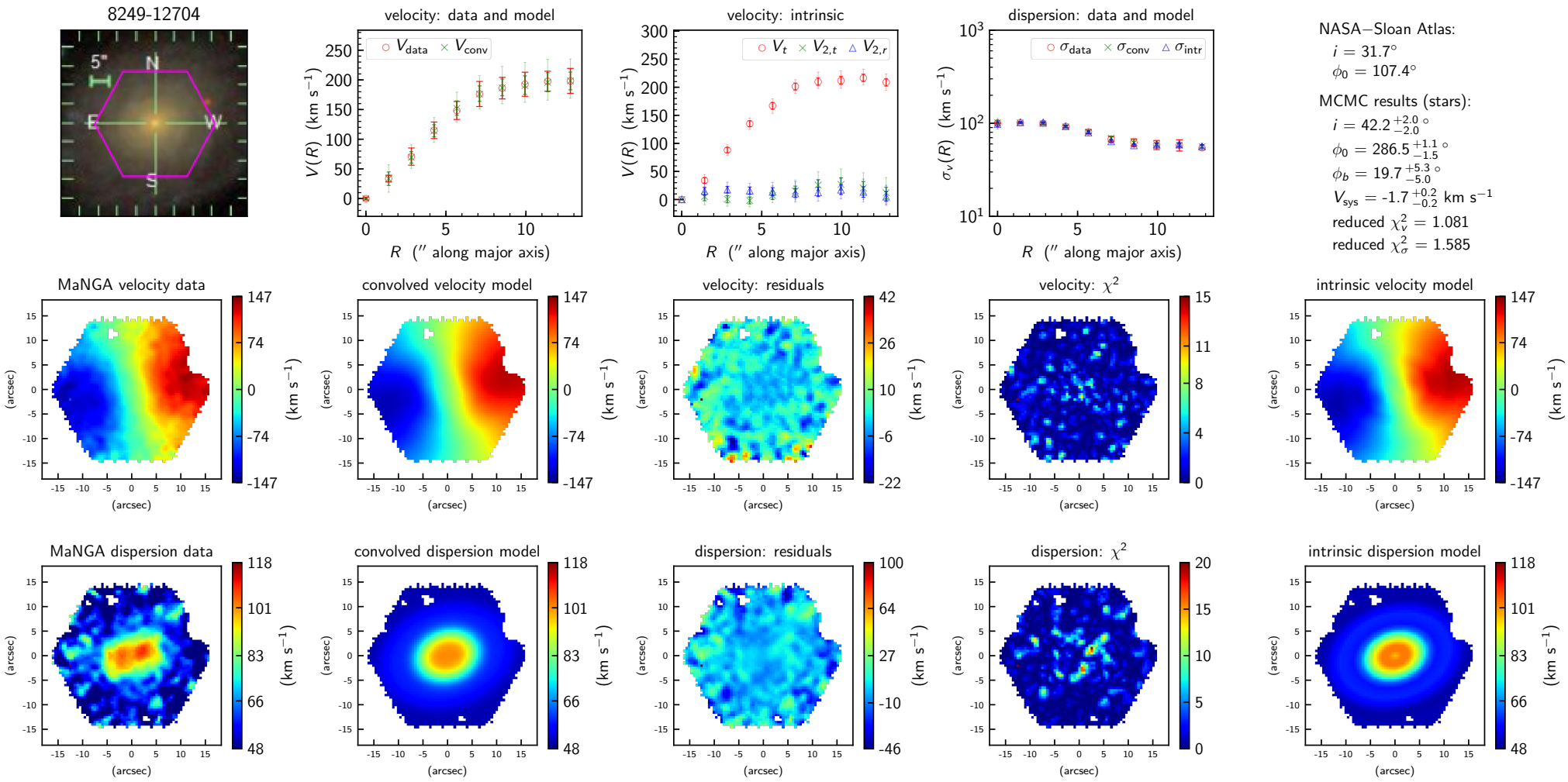

Figure 4.1 – MaNGA galaxy 8249-12704, **stars**. *Top row*: The top-left panel shows an SDSS optical image of the MaNGA galaxy. The pink hexagon indicates the spatial coverage of the MaNGA IFU instrument. The remaining panels in this row show the best-fit 1D intrinsic models; the data and convolved models are deprojected to 1D given the fitted values of disk inclination and position angles. The error bars on binned 1D model quantities represent 1σ (thick) and 2σ (thin) of the distributions sampled by MCMC. The models are defined in Section 3.1. The error bars on binned data (red) capture the measurement uncertainties reported for individual pixels assigned to a given bin *and* the variance of data in the bin, computed according to Equation 4.1. *Middle row*: 2D velocity data and fitted model. *Bottom row*: 2D velocity dispersion data and fitted model. Convolved models shown in the 2D rows are the results of convolving the intrinsic models with the observation's PSF, as described in Section 3.1.3. Model residuals and χ^2 compare data and convolved models.

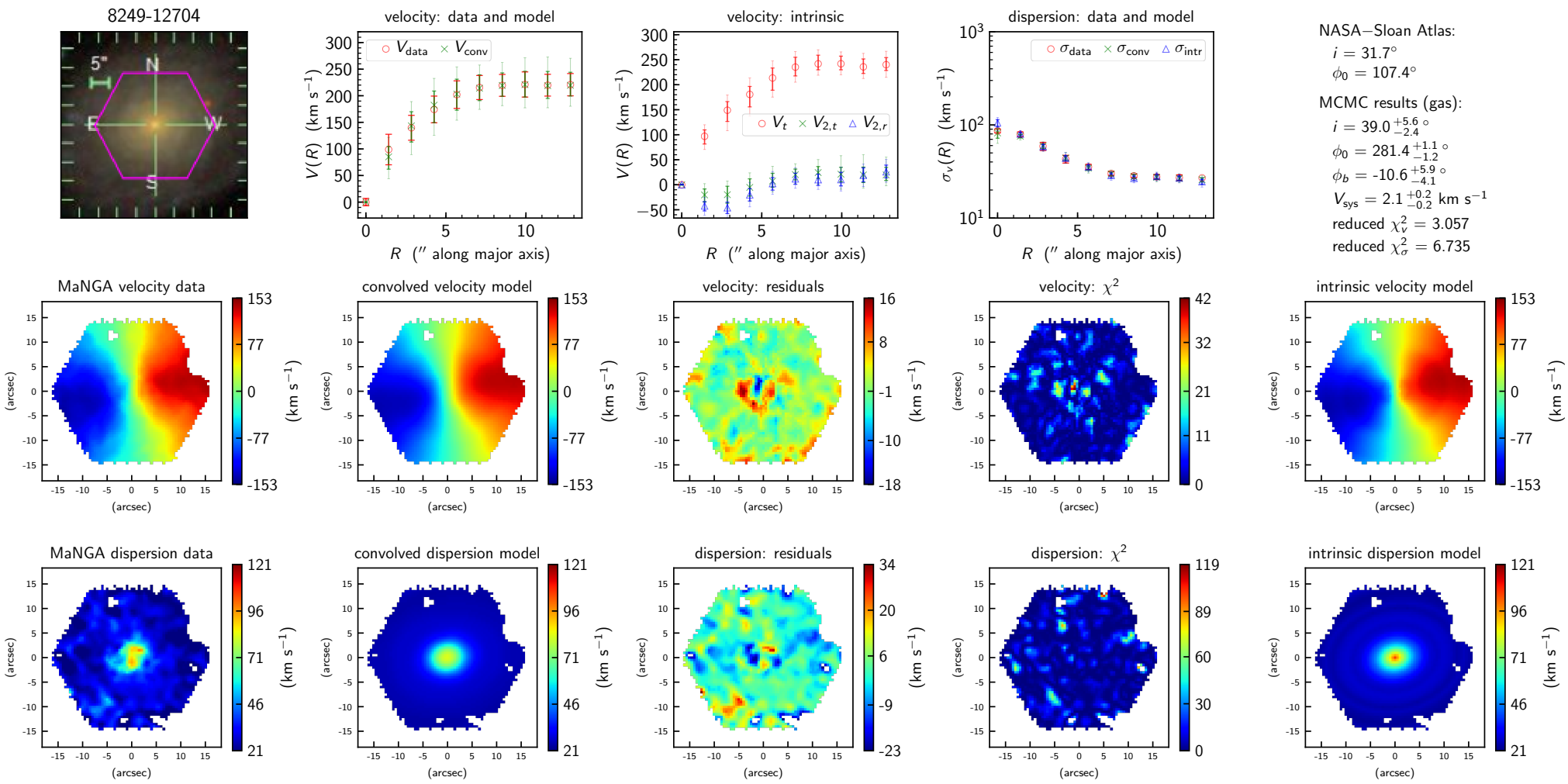

Figure 4.2 – MaNGA galaxy 8249-12704, **gas**. *Top row*: The top-left panel shows an SDSS optical image of the MaNGA galaxy. The pink hexagon indicates the spatial coverage of the MaNGA IFU instrument. The remaining panels in this row show the best-fit 1D intrinsic models; the data and convolved models are deprojected to 1D given the fitted values of disk inclination and position angles. The error bars on binned 1D model quantities represent 1σ (thick) and 2σ (thin) of the distributions sampled by MCMC. The models are defined in Section 3.1. The error bars on binned data (red) capture the measurement uncertainties reported for individual pixels assigned to a given bin *and* the variance of data in the bin, computed according to Equation 4.1. *Middle row*: 2D velocity data and fitted model. *Bottom row*: 2D velocity dispersion data and fitted model. Convolved models shown in the 2D rows are the results of convolving the intrinsic models with the observation's PSF, as described in Section 3.1.3. Model residuals and χ^2 compare data and convolved models.

4.1.2 A Disk with Distinct Velocity Components

Figures 4.3 and 4.4 show the data and fitted kinematic results for MaNGA galaxy 8715-12701. In SDSS optical imaging, this object appears to an Sa or Sb galaxy oriented at a moderately inclined angle. There appears to be a warp in the 2D MaNGA velocity map, with the warp more pronounced in the gas data than in the stellar data. Our code is able to reproduce this warp feature in the simulated observed velocity map, which is the result of the intrinsic velocity model convolved with the observation's PSF in accordance with Equation 3.9. Note that the $m = 2$ mode appears in the data as a twist in the isovelocity lines of the velocity field. Our MCMC-fitted kinematic results suggest that after the bisymmetric $m = 2$ motions are accounted for, the remaining mean tangential speed $\bar{V}_t$ appears to have two distinct components. The flattening out of the $\bar{V}$ rotation curve within $5''$ from the galaxy's center and the eventual resumption of the increasing trend appear to coincide with the visible gap feature in the optical image. The radii at which the $m = 2$ terms in the model reach their maximum amplitude appears to coincide with the location of the ring-like feature seen in the optical image, though further investigation is needed explain the offset between the $m = 2$ maxima in the stellar and gas models.

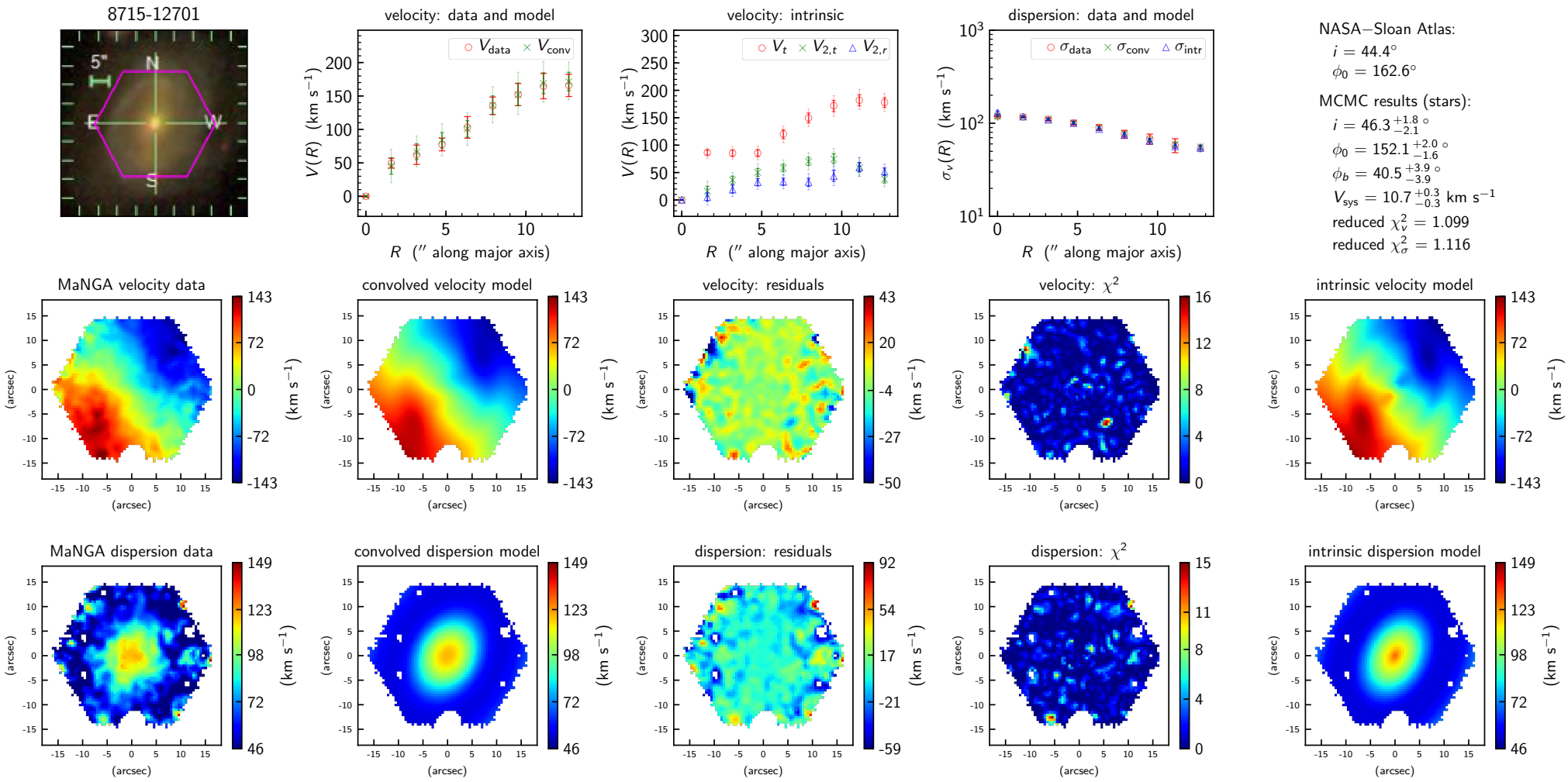

Figure 4.3 – MaNGA galaxy 8715-12701, **stars**. *Top row*: The top-left panel shows an SDSS optical image of the MaNGA galaxy. The pink hexagon indicates the spatial coverage of the MaNGA IFU instrument. The remaining panels in this row show the best-fit 1D intrinsic models; the data and convolved models are deprojected to 1D given the fitted values of disk inclination and position angles. The error bars on binned 1D model quantities represent 1σ (thick) and 2σ (thin) of the distributions sampled by MCMC. The models are defined in Section 3.1. The error bars on binned data (red) capture the measurement uncertainties reported for individual pixels assigned to a given bin *and* the variance of data in the bin, computed according to Equation 4.1. *Middle row*: 2D velocity data and fitted model. *Bottom row*: 2D velocity dispersion data and fitted model. Convolved models shown in the 2D rows are the results of convolving the intrinsic models with the observation's PSF, as described in Section 3.1.3. Model residuals and χ^2 compare data and convolved models.

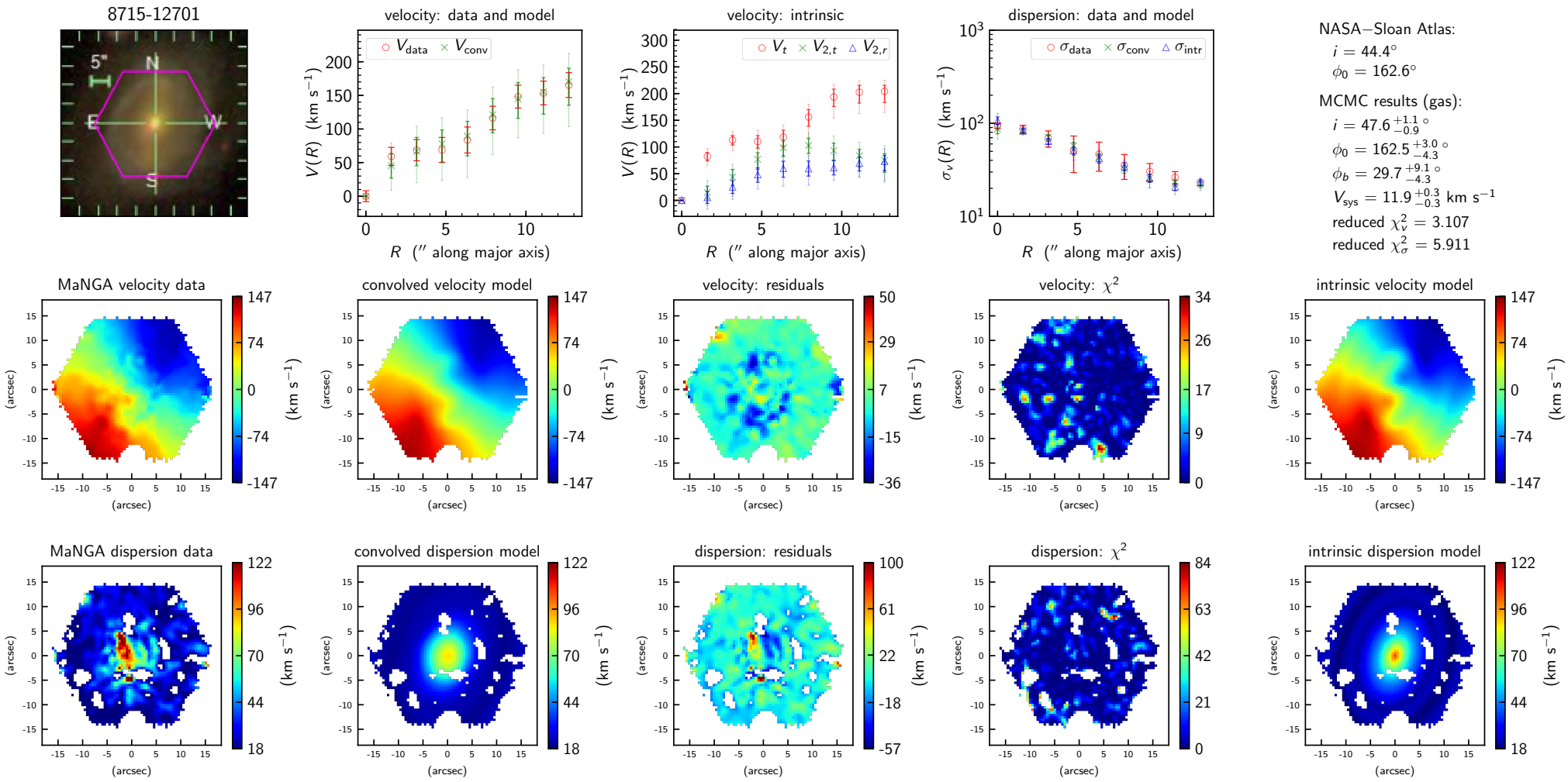

Figure 4.4 – MaNGA galaxy 8715-12701, **gas**. *Top row*: The top-left panel shows an SDSS optical image of the MaNGA galaxy. The pink hexagon indicates the spatial coverage of the MaNGA IFU instrument. The remaining panels in this row show the best-fit 1D intrinsic models; the data and convolved models are deprojected to 1D given the fitted values of disk inclination and position angles. The error bars on binned 1D model quantities represent 1σ (thick) and 2σ (thin) of the distributions sampled by MCMC. The models are defined in Section 3.1. The error bars on binned data (red) capture the measurement uncertainties reported for individual pixels assigned to a given bin *and* the variance of data in the bin, computed according to Equation 4.1. *Middle row*: 2D velocity data and fitted model. *Bottom row*: 2D velocity dispersion data and fitted model. Convolved models shown in the 2D rows are the results of convolving the intrinsic models with the observation's PSF, as described in Section 3.1.3. Model residuals and χ^2 compare data and convolved models.

4.1.3 A Strong Bar Feature

Figures 4.5 and 4.6 show the data and fitted kinematic results for MaNGA galaxy 8083-12704, a nearly face-on SBc galaxy. The fitted kinematic models for both stars and gas show $m = 2$ terms consistent with zero except for the inner-most $5''$, which correspond rather precisely to the extent of the prominent bar feature in the optical image. The $m = 2$ mode appears in the data as a twist in the isovelocity lines of the velocity field, with the twist more pronounced in the gas data.

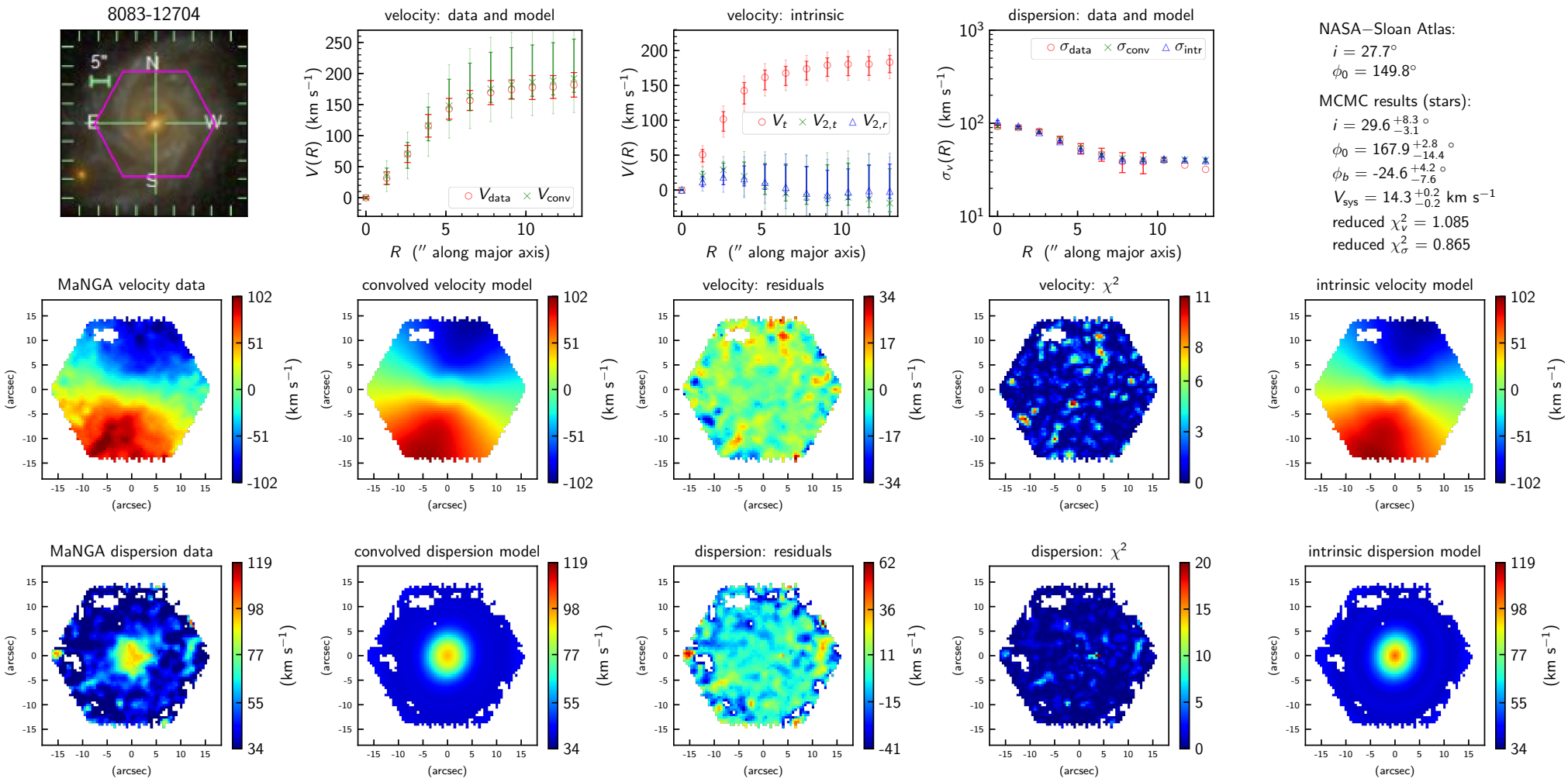

Figure 4.5 – MaNGA galaxy 8083-12704, **stars**. *Top row*: The top-left panel shows an SDSS optical image of the MaNGA galaxy. The pink hexagon indicates the spatial coverage of the MaNGA IFU instrument. The remaining panels in this row show the best-fit 1D intrinsic models; the data and convolved models are deprojected to 1D given the fitted values of disk inclination and position angles. The error bars on binned 1D model quantities represent 1σ (thick) and 2σ (thin) of the distributions sampled by MCMC. The models are defined in Section 3.1. The error bars on binned data (red) capture the measurement uncertainties reported for individual pixels assigned to a given bin *and* the variance of data in the bin, computed according to Equation 4.1. *Middle row*: 2D velocity data and fitted model. *Bottom row*: 2D velocity dispersion data and fitted model. Convolved models shown in the 2D rows are the results of convolving the intrinsic models with the observation's PSF, as described in Section 3.1.3. Model residuals and χ^2 compare data and convolved models.

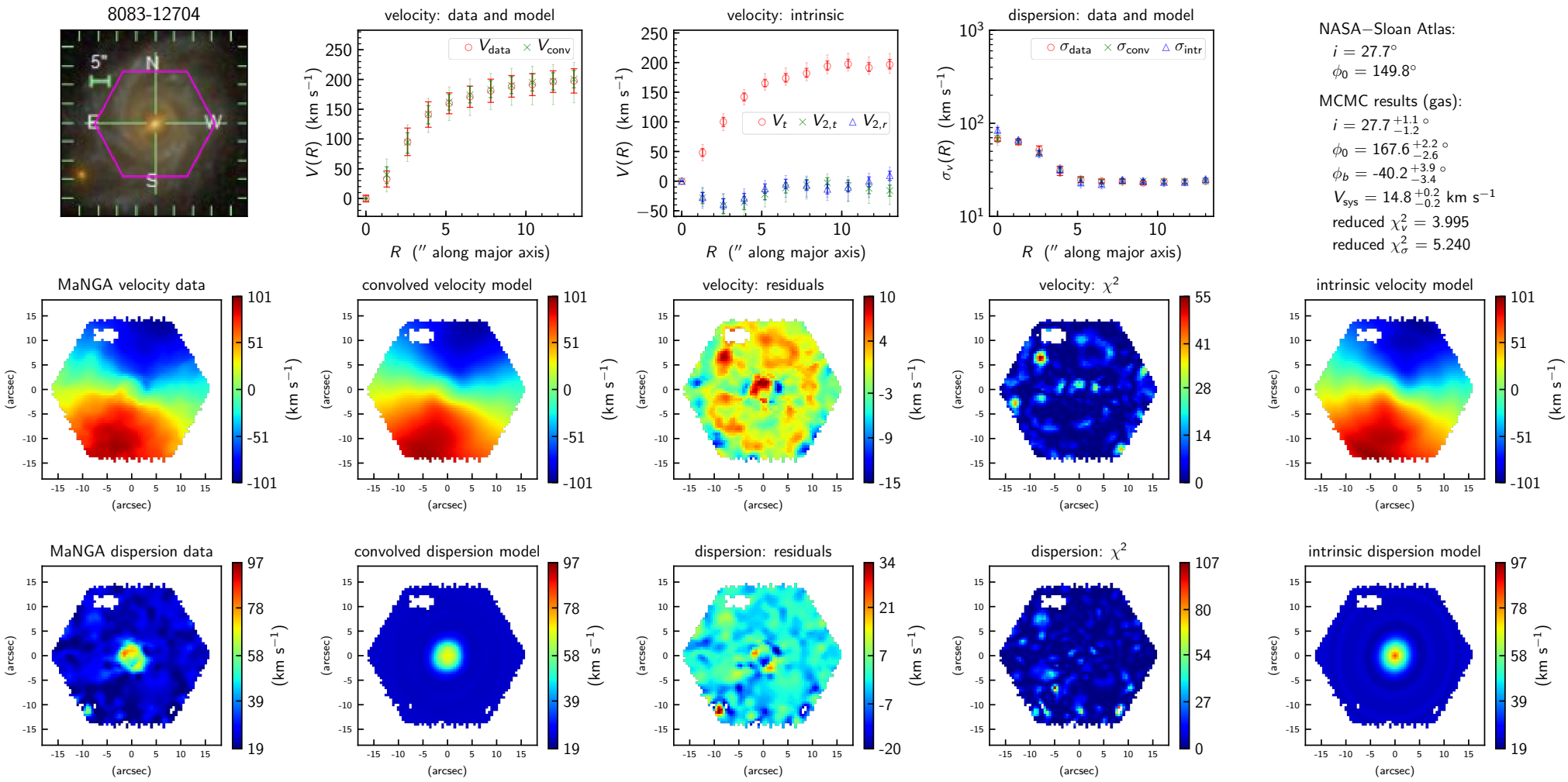

Figure 4.6 – MaNGA galaxy 8083-12704, **gas**. *Top row*: The top-left panel shows an SDSS optical image of the MaNGA galaxy. The pink hexagon indicates the spatial coverage of the MaNGA IFU instrument. The remaining panels in this row show the best-fit 1D intrinsic models; the data and convolved models are deprojected to 1D given the fitted values of disk inclination and position angles. The error bars on binned 1D model quantities represent 1σ (thick) and 2σ (thin) of the distributions sampled by MCMC. The models are defined in Section 3.1. The error bars on binned data (red) capture the measurement uncertainties reported for individual pixels assigned to a given bin *and* the variance of data in the bin, computed according to Equation 4.1. *Middle row*: 2D velocity data and fitted model. *Bottom row*: 2D velocity dispersion data and fitted model. Convolved models shown in the 2D rows are the results of convolving the intrinsic models with the observation's PSF, as described in Section 3.1.3. Model residuals and χ^2 compare data and convolved models.

4.1.4 Possible Dynamical Heating in Gas Disk

Figures 4.7 and 4.8 show the data and fitted kinematic results for MaNGA galaxy 8078-12703, a moderately inclined SBb galaxy. This is the first example we have presented that exhibits prominent differences in stellar kinematics versus gas kinematics. The differences are already discernible in the MaNGA kinematic data, the gas velocity map showing significantly more warped features than in the stellar velocity map. In the MCMC-fitted intrinsic models, the V_t rotation curve for gas shows two components, as we have seen in MaNGA galaxy 8715-12701 presented in Section . Strangely perhaps, this two-component feature is entirely absent from the MCMC-fitted stellar kinematics. The fitted $m = 2$ modes for stars and gas also exhibit very different profiles, complete with different fitted values for the bar axis. A possible explanation is the galaxy was subjected an event that dynamically heated the gas disk in recent past. The gas velocity dispersion matches the stellar velocity dispersion in the central region of the galaxy, suggesting not enough time has elapsed since the such as event for the gas to cool. Further investigation is required.

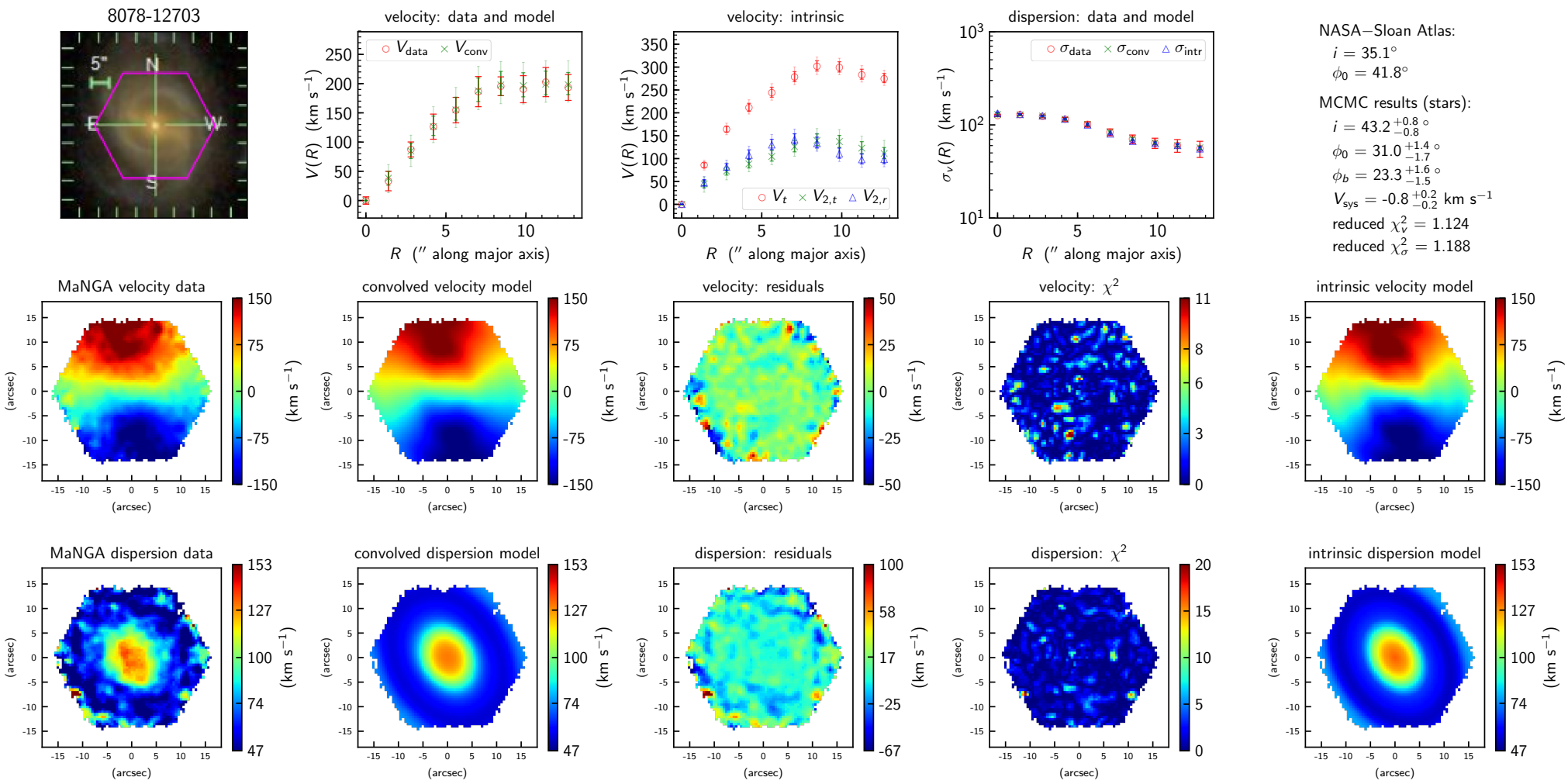

Figure 4.7 – MaNGA galaxy 8078-12703, **stars**. *Top row*: The top-left panel shows an SDSS optical image of the MaNGA galaxy. The pink hexagon indicates the spatial coverage of the MaNGA IFU instrument. The remaining panels in this row show the best-fit 1D intrinsic models; the data and convolved models are deprojected to 1D given the fitted values of disk inclination and position angles. The error bars on binned 1D model quantities represent 1σ (thick) and 2σ (thin) of the distributions sampled by MCMC. The models are defined in Section 3.1. The error bars on binned data (red) capture the measurement uncertainties reported for individual pixels assigned to a given bin *and* the variance of data in the bin, computed according to Equation 4.1. *Middle row*: 2D velocity data and fitted model. *Bottom row*: 2D velocity dispersion data and fitted model. Convolved models shown in the 2D rows are the results of convolving the intrinsic models with the observation's PSF, as described in Section 3.1.3. Model residuals and χ^2 compare data and convolved models.

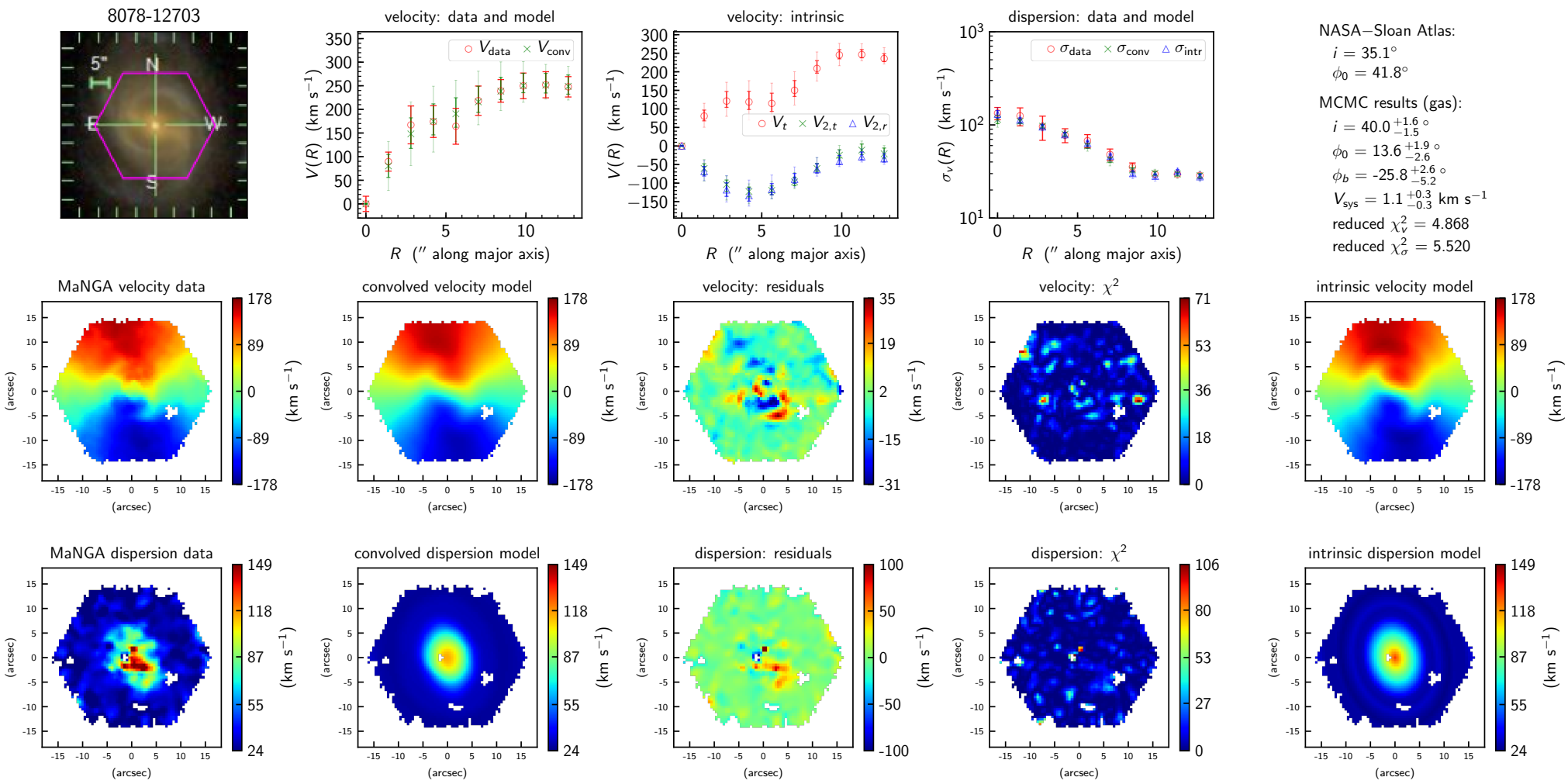

Figure 4.8 – MaNGA galaxy 8078-12703, **gas**. *Top row*: The top-left panel shows an SDSS optical image of the MaNGA galaxy. The pink hexagon indicates the spatial coverage of the MaNGA IFU instrument. The remaining panels in this row show the best-fit 1D intrinsic models; the data and convolved models are deprojected to 1D given the fitted values of disk inclination and position angles. The error bars on binned 1D model quantities represent 1σ (thick) and 2σ (thin) of the distributions sampled by MCMC. The models are defined in Section 3.1. The error bars on binned data (red) capture the measurement uncertainties reported for individual pixels assigned to a given bin *and* the variance of data in the bin, computed according to Equation 4.1. *Middle row*: 2D velocity data and fitted model. *Bottom row*: 2D velocity dispersion data and fitted model. Convolved models shown in the 2D rows are the results of convolving the intrinsic models with the observation's PSF, as described in Section 3.1.3. Model residuals and χ^2 compare data and convolved models.

4.1.5 Approaching Thin Disk Model's Limit

Figures 4.9 and 4.10 show the data and fitted kinematic results for MaNGA galaxy 8132-12704, a highly inclined disk galaxy. Our code was able to fit the stellar kinematic data, much to our delight and surprise. It was close to succeeding with the gas kinematic data, but for an actual feature in the central region of the galaxy but offset from the actual center. The feature is visible in the MaNGA gas velocity data as a disruption to the "spider diagram" pattern, and results in a prominent region of large model residuals.

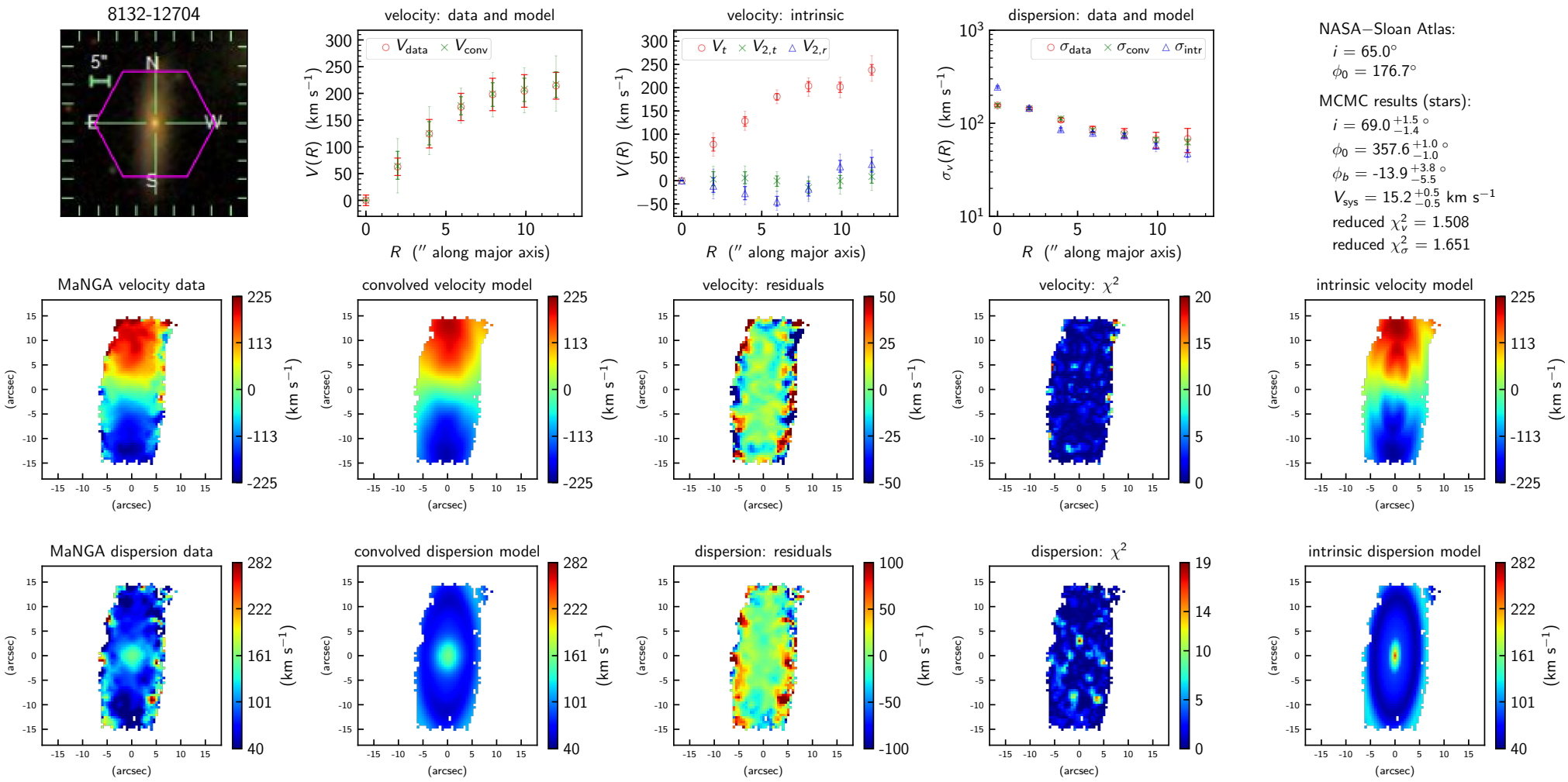

Figure 4.9 – MaNGA galaxy 8132-12704, **stars**. *Top row*: The top-left panel shows an SDSS optical image of the MaNGA galaxy. The pink hexagon indicates the spatial coverage of the MaNGA IFU instrument. The remaining panels in this row show the best-fit 1D intrinsic models; the data and convolved models are deprojected to 1D given the fitted values of disk inclination and position angles. The error bars on binned 1D model quantities represent 1σ (thick) and 2σ (thin) of the distributions sampled by MCMC. The models are defined in Section 3.1. The error bars on binned data (red) capture the measurement uncertainties reported for individual pixels assigned to a given bin *and* the variance of data in the bin, computed according to Equation 4.1. *Middle row*: 2D velocity data and fitted model. *Bottom row*: 2D velocity dispersion data and fitted model. Convolved models shown in the 2D rows are the results of convolving the intrinsic models with the observation's PSF, as described in Section 3.1.3. Model residuals and χ^2 compare data and convolved models.

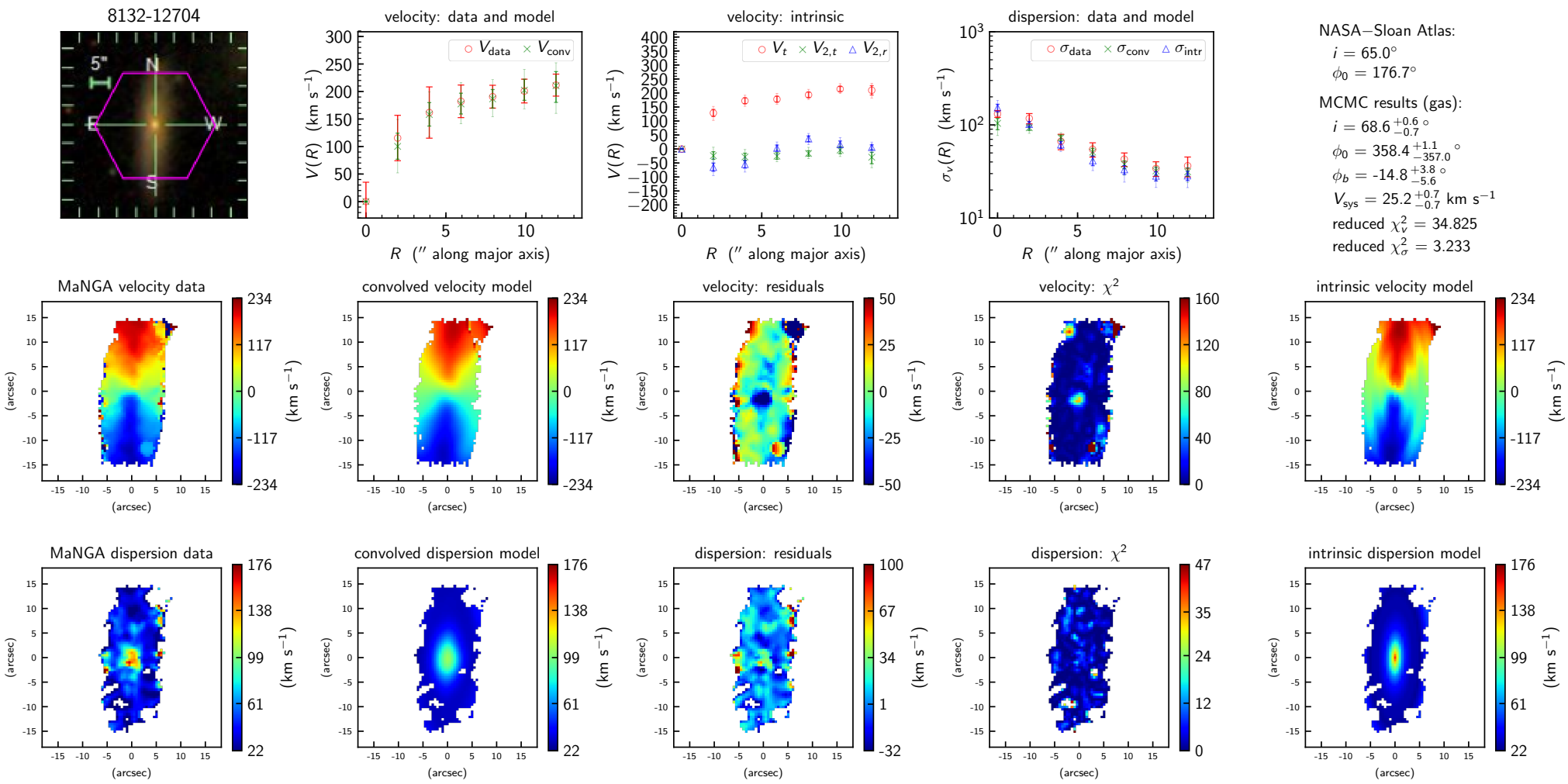

Figure 4.10 – MaNGA galaxy 8132-12704, **gas**. *Top row*: The top-left panel shows an SDSS optical image of the MaNGA galaxy. The pink hexagon indicates the spatial coverage of the MaNGA IFU instrument. The remaining panels in this row show the best-fit 1D intrinsic models; the data and convolved models are deprojected to 1D given the fitted values of disk inclination and position angles. The error bars on binned 1D model quantities represent 1σ (thick) and 2σ (thin) of the distributions sampled by MCMC. The models are defined in Section 3.1. The error bars on binned data (red) capture the measurement uncertainties reported for individual pixels assigned to a given bin *and* the variance of data in the bin, computed according to Equation 4.1. *Middle row*: 2D velocity data and fitted model. *Bottom row*: 2D velocity dispersion data and fitted model. Convolved models shown in the 2D rows are the results of convolving the intrinsic models with the observation's PSF, as described in Section 3.1.3. Model residuals and χ^2 compare data and convolved models.

4.1.6 Common Failure Modes

4.1.6.1 Convergence but Unphysical

For the reasons discussed in Section 3.3, we do not expect our code with the current models to be able to fit highly inclined disks. Figure 4.12 shows an example of such a failure. While the reported χ^2 is reasonably small and $\hat{r}$ indicating convergence (though not anywhere close to 1), a visual inspection of the intrinsic models in Figure 4.12 reveals that the model is unphysical, with the kinematic major axis pointing out of the disk plane of the galaxy.

The MCMC code has minimized the χ^2 as best it could without regard to the model's physical interpretation. The $m = 2$ mode velocity terms in the kinematic model, in conjunction with an incorrect value of ϕ_0, are able to produce a velocity map that mimics the data. Figure 4.11 shows kinematic models produced during attempts to fit two other galaxies with similarly extreme inclination angles. With the MaNGA data masks removed from the images showing the intrinsic velocity field (top left in each frame), we can see just how much the $m = 2$ modes have warped the velocity field, and how convolution with the PSF (which smooths out the small features) and the application of the data mask (top right) can allow the simulated observation to mimic the data (bottom left).

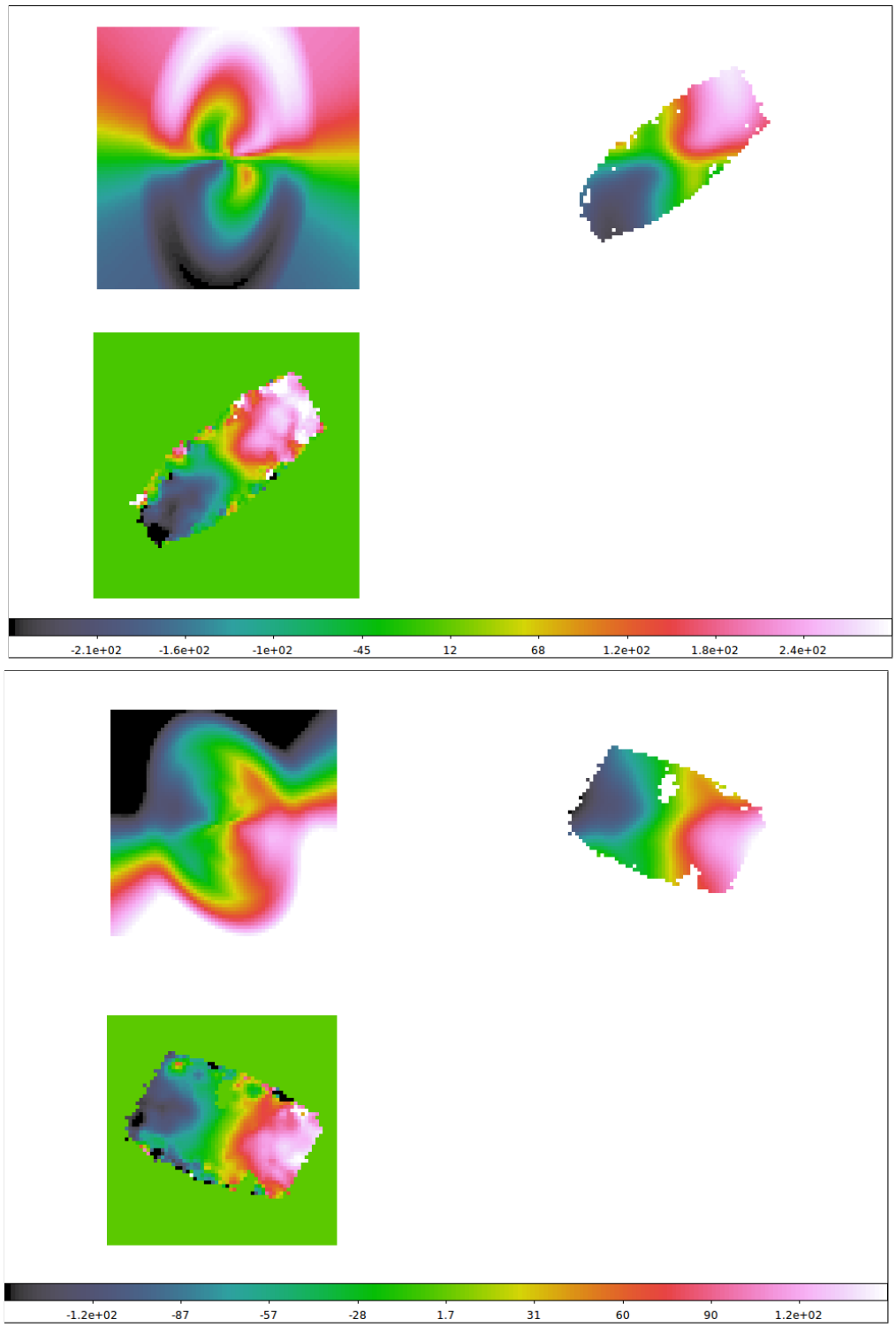

Figure 4.11 – The intrinsic velocity map (shown in the *top left* in each frame) combines strong nonaxisymmetric modes with an unphysical disk position angle, such that when it is convolved with the reconstructed PSF and with same data mask applied (*top right* in each frame), mimics a good fit to the MaNGA data (*bottom left* in each frame). The models and data shown in the top frame correspond to MaNGA galaxy 8329-12702; bottom frame shows MaNGA galaxy 8145-9101.

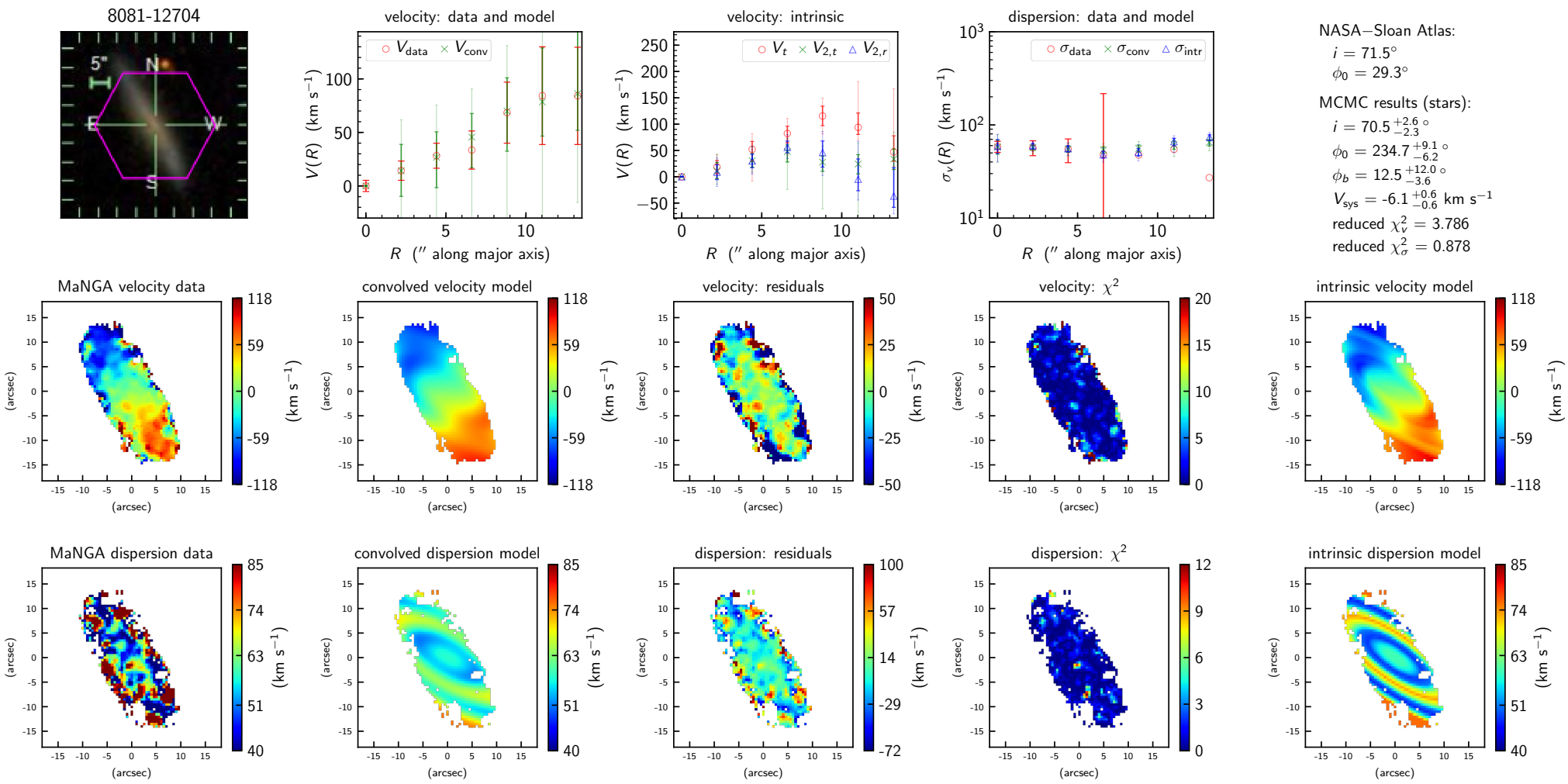

Figure 4.12 – MaNGA galaxy 8081-12704, **stars**. *Top row*: The top-left panel shows an SDSS optical image of the MaNGA galaxy. The pink hexagon indicates the spatial coverage of the MaNGA IFU instrument. The remaining panels in this row show the best-fit 1D intrinsic models; the data and convolved models are deprojected to 1D given the fitted values of disk inclination and position angles. The error bars on binned 1D model quantities represent 1σ (thick) and 2σ (thin) of the distributions sampled by MCMC. The models are defined in Section 3.1. The error bars on binned data (red) capture the measurement uncertainties reported for individual pixels assigned to a given bin *and* the variance of data in the bin, computed according to Equation 4.1. *Middle row*: 2D velocity data and fitted model. *Bottom row*: 2D velocity dispersion data and fitted model. Convolved models shown in the 2D rows are the results of convolving the intrinsic models with the observation's PSF, as described in Section 3.1.3. Model residuals and χ^2 compare data and convolved models.

4.1.6.2 Failure to Converge

A pure thin disk model is not suited for modeling disk galaxy oriented in at a highly inclined angle (Section 3.3). Figure 4.13 shows an attempt to fit the gas kinematic data for the MaNGA galaxy 8081-12704, the same galaxy shown in Figure 4.12. The fit shown here never converged, with unreasonable (huge) model velocities just outside the range of the 1D intrinsic velocity model figure that is skewing the automated scaling of the vertical axis. We can observe this failure in the 2D models, residuals and χ^2.

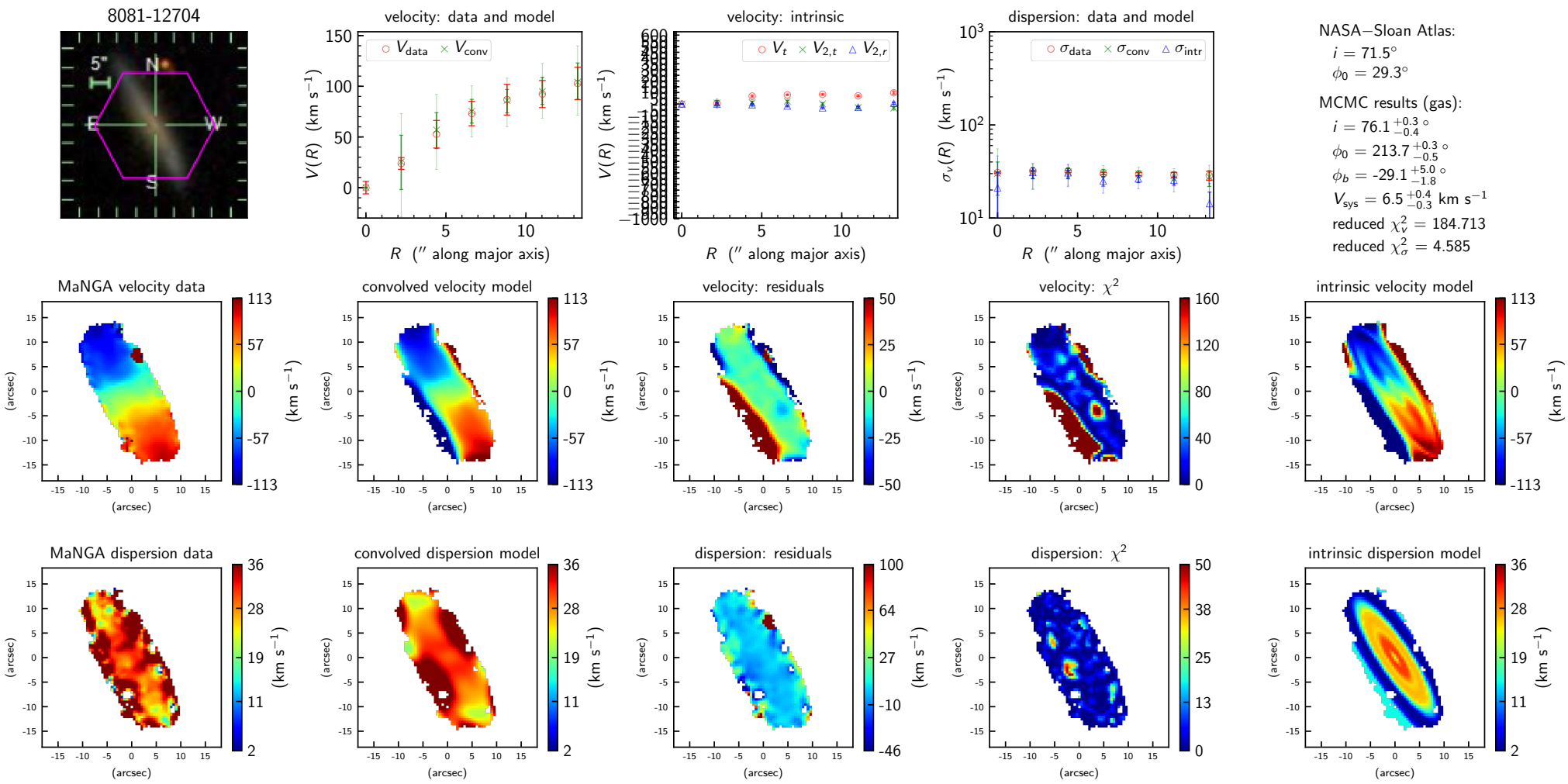

Figure 4.13 – MaNGA galaxy 8081-12704, **gas**. *Top row*: The top-left panel shows an SDSS optical image of the MaNGA galaxy. The pink hexagon indicates the spatial coverage of the MaNGA IFU instrument. The remaining panels in this row show the best-fit 1D intrinsic models; the data and convolved models are deprojected to 1D given the fitted values of disk inclination and position angles. The error bars on binned 1D model quantities represent 1σ (thick) and 2σ (thin) of the distributions sampled by MCMC. The models are defined in Section 3.1. The error bars on binned data (red) capture the measurement uncertainties reported for individual pixels assigned to a given bin *and* the variance of data in the bin, computed according to Equation 4.1. *Middle row*: 2D velocity data and fitted model. *Bottom row*: 2D velocity dispersion data and fitted model. Convolved models shown in the 2D rows are the results of convolving the intrinsic models with the observation's PSF, as described in Section 3.1.3. Model residuals and χ^2 compare data and convolved models.

4.2 Asymmetric Drift

Any potential (Φ) can be characterized by its circular speed, $V_c(R)$. Stars often have significant dispersion (even in disks), so they don't rotate at the local circular speed of Φ. On the other hand, gas has little dispersion because it is collisional and dissipative, and so gas traces the local circular speed of Φ. The difference between local circular speed and mean tangential speed of stellar population is called asymmetric drift (Binney & Tremaine 2008; Golubov et al. 2013).

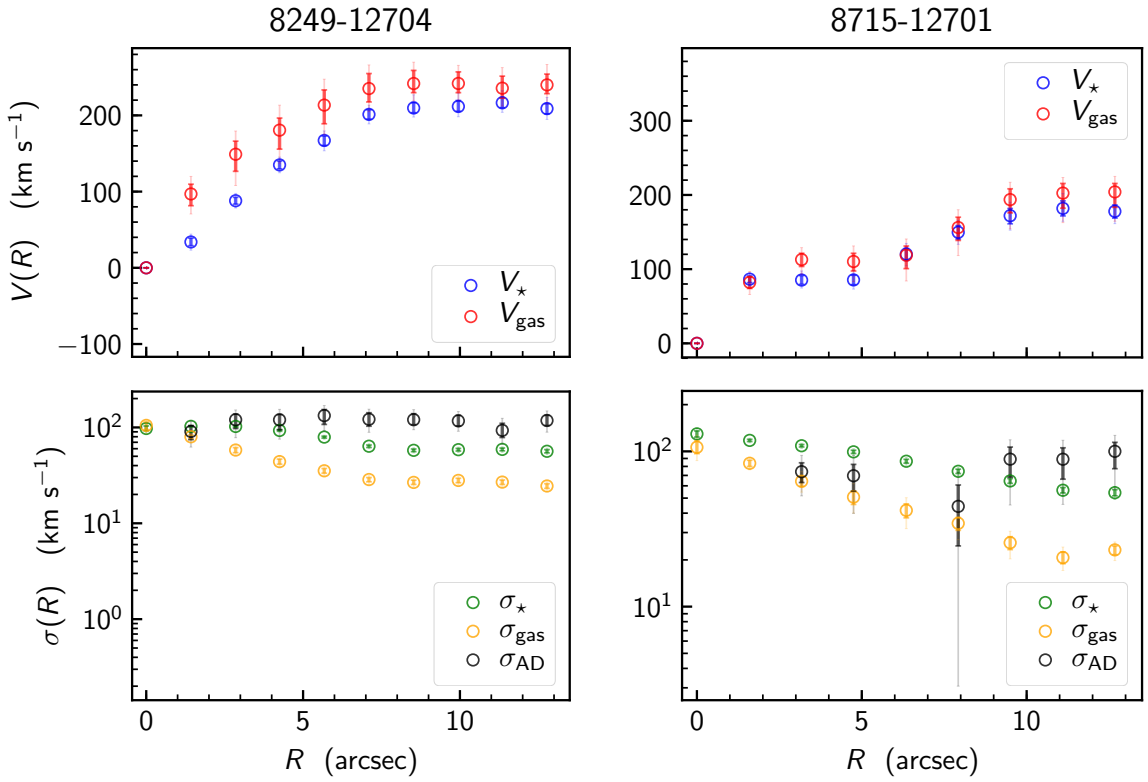

Figure 4.14 – Asymmetric drift for two galaxies based on modeled intrinsic kinematics. *Left panels*: MaNGA galaxy 8249-12704; see also Figures 4.1 and 4.2. *Right panels*: MaNGA galaxy 8715-12701; see also Figures 4.3 and 4.4. *Top panels*: Intrinsic tangential speed of stellar and gas components; see Section 4.2 for a discussion of caveats. *Bottom panels*: Asymmetric drift, $\sigma^2_{\rm AD} \equiv V^2_{\rm gas} - V^2_\star$, and intrinsic velocity dispersions of stars and gas components. The error bars on binned 1D model quantities represent 1σ (thick) and 2σ (thin) of the distributions sampled by MCMC. Error bars on $\sigma_{\rm AD}$ are propagated from those on $V_{\rm gas}$ and $V_\star$ in quadrature.

$\bar{V}_t(R)$ for gas may be interpreted as the local circular speed of the potential at radius R, provided that the $m = 2$ mode terms are comparatively small. $\bar{V}_t(R)$ for stars is the mean tangential velocity of stellar population. Figure 4.14 shows the mean tangential speeds for the stellar and gas

components of two galaxies. For our analysis, we quantify asymmetric drift as follows:

$$\sigma^2_{\rm AD} \equiv \bar{V}^2_{t,\rm gas} - \bar{V}^2_{t,\star}\,. \tag{4.2}$$

Since bar-like or oval distortions are captured by the $m = 2$ terms in the bisymmetric model, $\bar{V}_t(R)$ represents the rotational motion in the tangential direction for local stellar populations. If $\bar{V}_{t,\rm gas}$ is an accurate representation of the circular speed at a radius R due to the the potential and $\bar{V}_{t,\star}$ captures the mean circular motion of stellar populations local to radius R, absent $m > 0$ distortions to the potential, then $\sigma^2_{\rm AD}$ in Equation 4.2 is equivalent to the expression on either side of the asymmetric drift equation (Binney & Tremaine 2008):[2]

$$v_c^2 - \bar{v}_\phi^2 = \sigma_\phi^2 - \sigma_R^2 - \frac{R}{\rho}\frac{\partial(\rho\sigma_R^2)}{\partial R} - R\,\frac{\partial(\overline{v_R v_z})}{\partial z}\,. \tag{4.3}$$

Culling the sample. The sample of $\sim$ 400 galaxies is culled for the following conditions: $\hat{r} < 2$ for all fitted parameters (Section 3.2.6); the kinematic disk inclination angle is within 15° of the inclination reported in the NASA–Sloan Atlas (NSA; Blanton et al. 2011) obtained via SDSS imaging.

Figure 4.16 shows the trend in $\sigma_{\rm AD}$ versus D_n4000, the 4000Å break spectral index, for ~ 250 galaxies in the culled sample. Each point in this figure represents a radial bin from a galaxy in the culled sample that satisfy two additional conditions: $V_{\rm gas}(R) > V_\star(R)$, so that $\sigma_{\rm AD}(R)$ is a real-valued quantity; $m = 2$ mode coefficients are comparatively small ($< 0.4\times$ the coefficient on the corresponding $m = 0$ term, the mean tangential speed) for both kinematic components.

4.3 Tully–Fisher Relation

Taking the average value of $\bar{V}_t$ in the flat portion of the gas rotation curve to represent the circular speed of each galaxy, we show the Tully–Fisher relation (TFR) in Figure 4.15, plotting stellar mass (NSA catalog) versus V_c for ~ 200 disk galaxies in MaNGA (~ 50 galaxies in the culled sample do not exhibit flat $\bar{V}_t$ rotation curve in their gas component within the MaNGA IFU's spatial

[2]The asymmetric drift equation derives from the collisionless Boltzmann equation with the assumptions of steady state and axisymmetry.

coverage). We fit a straight line by Deming regression, which minimizes residuals perpendicular to the fitted line, and obtained a slope of 3.9, consistent with values reported by previous studies of the stellar mass TFR (McGaugh et al. 2000; Bloom et al. 2017).

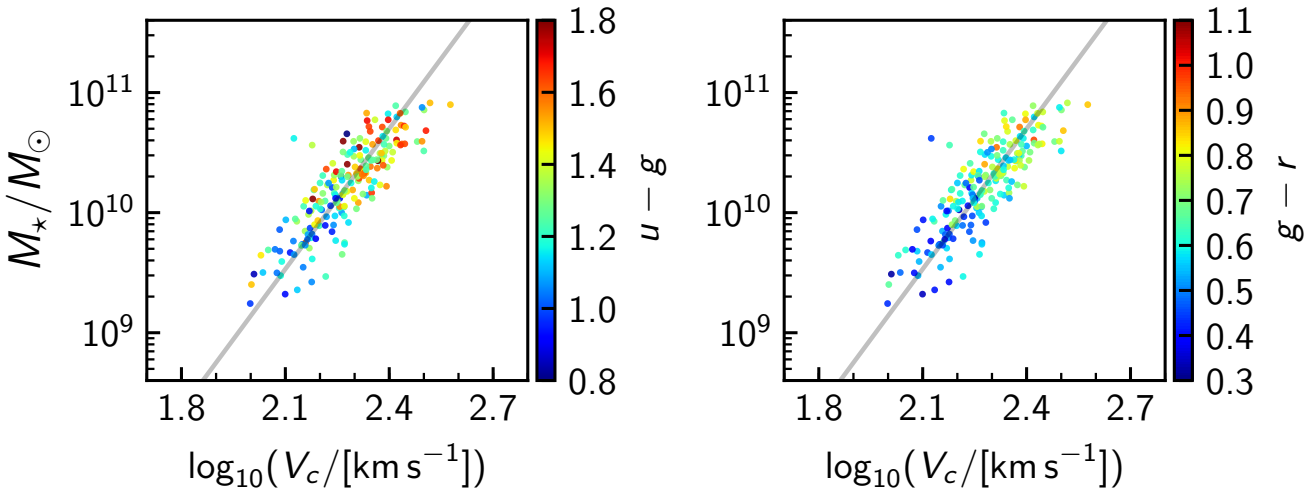

Figure 4.15 – Stellar mass Tully–Fisher relation for ~ 200 disk galaxies in MaNGA. We report a slope of 3.9 by fitting a straight line by Deming regression, which minimizes residuals perpendicular to the fitted line. Each point represents a MaNGA disk galaxy whose MCMC-fit results satisfy the conditions given in Section 4.2. The color of each point indicate the color index (*left panel*: $u-g$; *right panel*: $g-r$) of the galaxy reported in the NSA catalog.

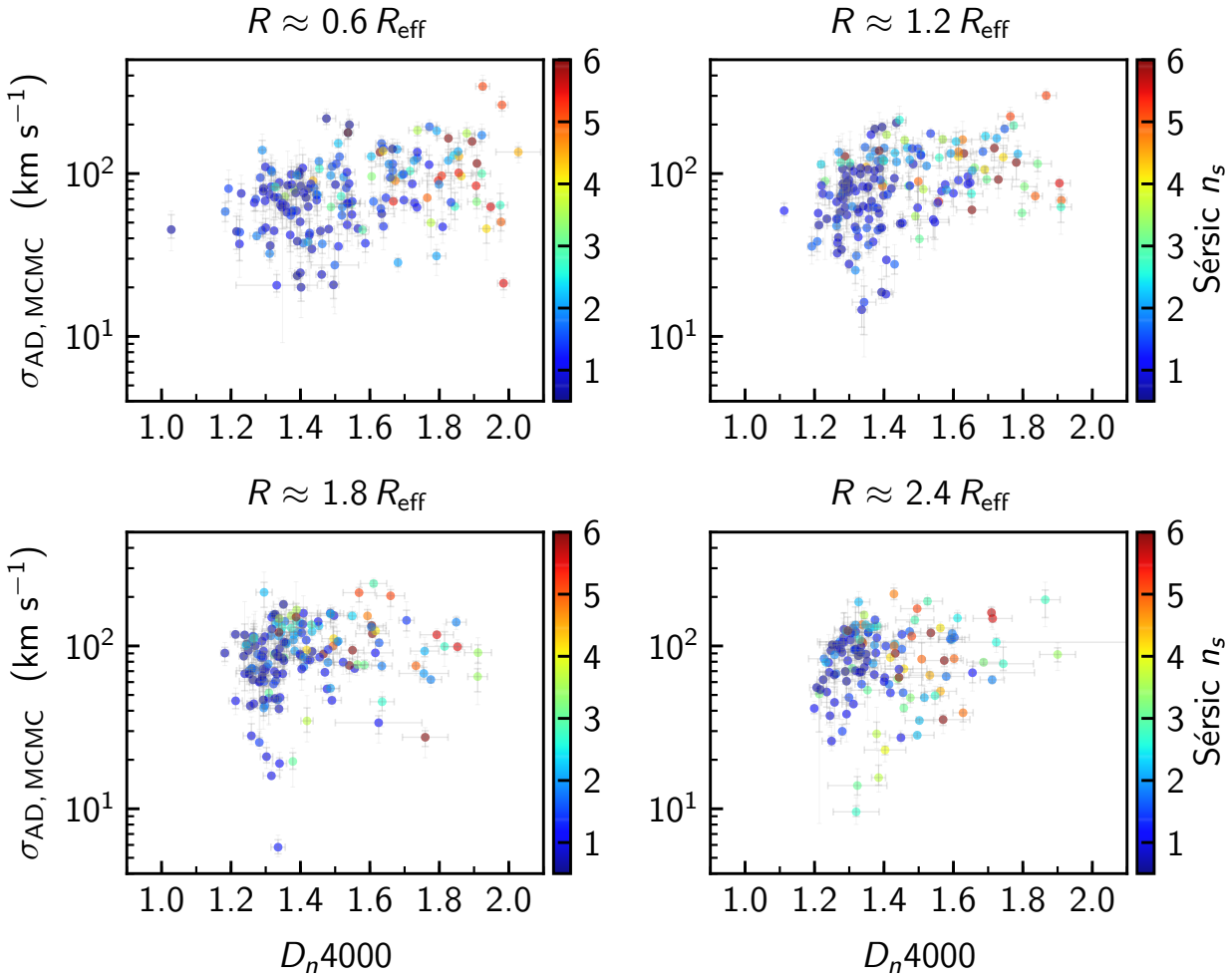

Figure 4.16 – Asymmetric drift represented by $\sigma_{\rm AD}$ (Equation 4.2) inferred from MCMC-fitted intrinsic tangential velocities of stars and gas components (see Section 4.2) plotted against D_n4000 for ~ 250 disk galaxies in MaNGA. Each point represents a radial bin from an MCMC-fitted galaxy. The separate panels compile only the results for the specified regions relative to each galaxy's effective radius (R_e). Only radial bins for which $V_{\rm gas} > V_\star$ (i.e., for which $\sigma_{\rm AD}$ is real-valued) are shown. The color of each point indicates the Sérsic index (n_s) of the galaxy to which the binned data belong.

Chapter 5

Conclusion

Kinematic maps derived from spatially resolved spectroscopic data obtained by the ManGA survey will provide a sample unprecedented in its combination of size and spatial resolution. This statistical power of the MaNGA sample allows us to study the correlations between various physical or spectral properties (e.g., $M_\star$, V_c, Υ, D_n4000, n_s) and the kinematic structure of galaxies ($V_t(R)$, $\sigma_V(R)$, etc.).

Beam smearing and atmospheric seeing are the dominant effects captured by the PSFs reconstructed for each observation by the MaNGA DRP (Law et al. 2016). The removal of these effects from the kinematic data is essential for accurate dynamical models. Forward modeling overcomes the impracticality of deconvolution by identifying the most probable model given the data and the PSF. By simulating what the instrument does, this method takes a kinematic model from intrinsic to data space.

The results on a small sample demonstrates the ability of the MCMC forward modeling code described in Section 3.2 to extract intrinsic kinematic models from seeing-degraded data. This sample was selected (Section 3.3) to be suitable for a thin disk model. The intrinsic kinematics extracted by this MCMC code using a bisymmetric model (Section 3.1) have allowed us to quantify asymmetric drift and reproduce the stellar mass Tully–Fisher relation with limited scatter. The mean tangential speed of the gas component, with bisymmetric perturbations to the potential accurately accounted for and captured by second-order terms, enables robust determination of the radial mass profile for each modeled galaxy in further investigation.

Bibliography

Andersen, D. R., & Bershady, M. A. 2013, *Astrophys. J.*, 768, 41

Binney, J., & Tremaine, S. 2008, Galactic Dynamics: Second Edition (Princeton, NJ: Princeton University Press)

Blanton, M. R., Kazin, E., Muna, D., Weaver, B. A., & Price-Whelan, A. 2011, *Astron. J*, 142, 31

Blanton, M. R., Bershady, M. A., Abolfathi, B., et al. 2017, *Astron. J*, 154, 28

Bloom, J. V., Croom, S. M., Bryant, J. J., et al. 2017, *Mon. Not. R. Astron. Soc.*, 472, 1809

Bottema, R. 1993, *Astron. Astrophys.*, 275, 16

Bundy, K., Bershady, M. A., Law, D. R., et al. 2015, *Astrophys. J.*, 798, 7

Cappellari, M., & Emsellem, E. 2004, *Publ. Astron. Soc. Pacific*, 116, 138

Cherinka, B., Sánchez-Gallego, J., Andrews, B., & Brownstein, J. 2018, sdss/marvin: Marvin Beta 2.2.0, doi:10.5281/zenodo.1146705

Courteau, S., Cappellari, M., de Jong, R. S., et al. 2014, *Rev. Mod. Phys.*, 86, 47

Dalcanton, J. J., & Stilp, A. M. 2010, *Astrophys. J.*, 721, 547

Davies, R., Förster Schreiber, N. M., Cresci, G., et al. 2011, *Astrophys. J.*, 741, 69

D'Onghia, E. 2015, *Astrophys. J. Letters*, 808, L8

Drory, N., MacDonald, N., Bershady, M. A., et al. 2015, *Astron. J*, 149, 77

Gelman, A., & Shirley, K. 2011, in Handbook of Markov Chain Monte Carlo: First Edition, ed. S. Brooks, A. Gelman, G. L. Jones, & X.-L. Meng (Boca Raton, FL: Chapman & Hall/CRC), 163–174

Gerssen, J., Kuijken, K., & Merrifield, M. R. 1997, *Mon. Not. R. Astron. Soc.*, 288, 618

Golubov, O., Just, A., Bienaymé, O., et al. 2013, *Astron. Astrophys.*, 557, A92

Ivezić, Ž., Connelly, A. J., VanderPlas, J. T., & Gray, A. 2014, Statistics, Data Mining, and Machine Learning in Astronomy (Princeton, NJ: Princeton University Press)

Krajnović, D., Cappellari, M., de Zeeuw, P. T., & Copin, Y. 2006, *Mon. Not. R. Astron. Soc.*, 366, 787

Law, D. R., Cherinka, B., Yan, R., et al. 2016, *Astron. J*, 152, 83

McGaugh, S. S., Schombert, J. M., Bothun, G. D., & de Blok, W. J. G. 2000, *Astrophys. J. Letters*, 533, L99

Noordermeer, E., Merrifield, M. R., & Aragón-Salamanca, A. 2008, *Mon. Not. R. Astron. Soc.*, 388, 1381

Press, W. H., Flannery, B. P., & Teukolsky, S. A. 2007, Numerical Recipes. The Art of Scientific Computing: Third Edition (Cambridge, England: Cambridge University Press)

Roberts, G. O., Gelman, A., & Gilks, W. R. 1997, *Ann. Appl. Probab.*, 7, 110

Sánchez-Blázquez, P., Peletier, R. F., Jiménez-Vicente, J., et al. 2006, *Mon. Not. R. Astron. Soc.*, 371, 703

Spekkens, K., & Sellwood, J. A. 2007, *Astrophys. J.*, 664, 204

Swendsen, R. H., & Wang, J.-S. 1986, Phys. Rev. Lett., 57, 2607

Varidel, M., Pracy, M., Croom, S., Owers, M. S., & Sadler, E. 2016, *Publ. Astron. Soc. Australia*, 33, e006

Vousden, W. D., Farr, W. M., & Mandel, I. 2016, *Mon. Not. R. Astron. Soc.*, 455, 1919

Wake, D. A., Bundy, K., Diamond-Stanic, A. M., et al. 2017, *Astron. J*, 154, 86